Strathprints Institutional Repository

This version is available at http://strathprints.strath.ac.uk/54318/

Two-equation and multi-fluid turbulence models for Rayleigh-Taylor mixing

Kokkinakis,I.W. and Drikakis,D.*

Cranfield University, Bedforshire MK43 0AL, United Kingdom

Youngs,D.L. and Williams,R.J.R.

AWE, Aldermaston, Reading RG7 4PR, United Kingdom

Abstract

This paper presents a new, improved version of the K-L model, as well as a detailed investigation of K-L and multi-fluid models with reference to high-resolution implicit large eddy simulations of compressible Rayleigh-Taylor mixing. The accuracy of the models is examined for different interface pressures and specific heat ratios for Rayleigh-Taylor flows at initial density ratios *3:1* and *20:1*. It is shown that the original version of the K-L model requires modifications in order to provide comparable results to the multi-fluid model. The modifications concern the addition of an enthalpy diffusion term to the energy equation; the formulation of the turbulent kinetic energy (source) term in the K equation; and the calculation of the local Atwood number. The proposed modifications significantly improve the results of the K-L model, which are found in good agreement with the multi-fluid model and Implicit Large Eddy Simulations with respect to the self-similar mixing width; peak turbulent kinetic energy growth rate, as well as volume fraction and turbulent kinetic energy profiles. However, a key advantage of the two-fluid model is that it can represent the degree of molecular mixing in a direct way, by transferring mass between the two phases. The limitations of the single-fluid K-L model as well as the merits of more advanced Reynolds-Averaged Navier-Stokes models are also discussed throughout the paper.

---

*Electronic address: d.drikakis@cranfield.ac.uk

I. INTRODUCTION

Rayleigh-Taylor (RT) instability and mixing occurs in a range of variable-density techno-logical flows such as inertial confinement fusion [1], cavitation [2] and combustion [3], as well as geophysical flows [4]. Geological flow examples include include oil trapping in salt-domes, atmospheric and oceanic flows, e.g, atmospheric temperature inversions and the formation of cirrus clouds. In astrophysics, the formation and development of nebulae and supernovae are also associated with RT instabilities [5–7]. A related process, Richtmyer-Meshkov (RM) instability occurs in variable-density flows when shock waves are present. For high-Reynolds number flows these instabilities can give rise to turbulent mixing and accurate modeling of RT/RM induced turbulence is often a major uncertainty in calculating behavior.

Despite the advances in computer hardware, direct numerical simulation (DNS) for complex applications will remain impracticable at least in the foreseeable future. As a result, Implicit Large Eddy Simulation (ILES) has been widely used for studying RM and RT mixing [8–12]. ILES combines the ability to directly capture strong shock waves and large flow scales associated with transition and turbulence at material interfaces without resorting to subgrid scale models. Although significant progress has been achieved in ILES methods, the approach is still computationally expensive for complex engineering applications at high Reynolds numbers. For such problems, turbulence models based on transport equations that predict the "average" behavior of the turbulent mixing zone, can be used. These equations allow larger time steps and coarser computational grids than ILES. However, due to the ensemble averaging of second- and higher-order correlations of turbulent fluctuations, additional terms arise that require the use of turbulence models.

Turbulence modeling of RM and RT mixing encompasses several challenges. In addition to the shock waves and material discontinuities, turbulent mixing features baroclinic effects as well as anisotropy and inhomogeneity resulting from initial and boundary conditions. The modeling assumptions and closure coefficients are validated and calibrated, respectively, through comparisons with experiments but also increasingly through comparisons with high-resolution large eddy and direct numerical simulations.

Turbulence models for compressible mixing can be classified in three categories. The simplest type of model uses ordinary differential equations for the width of the RT/RM mixing layer, where the bubble or spike amplitudes are described by balancing inertia,

buoyancy and drag forces; these are called buoyancy drag models [13–17]. These models are of limited use as they cannot model multiple mixing interfaces, cannot be easily extended to two and three dimensions and cannot address de-mixing (reduction of total fluid masses within the mixing zone); this can occur when there is a reversal in the pressure gradient and there is not complete mixing at a molecular level within the mixing zone.

To resolve these problems, a second category of models has been proposed, the so-called two-fluid (or multi-fluid models) [18–21] and references therein. These models use one set of equations for each fluid in addition to mean flow equations. The models are fairly complex but provide an accurate modeling framework for de-mixing and capture correctly the relative motion of the different fluid fragments. Finally, an intermediate class of models, which are significantly simpler than the two-fluid models, maintains the individual species fraction but assigns a single velocity for the mixture. The above models are also known as two-equation turbulence models because they consist of evolutionary equations for the turbulent kinetic energy per unit mass and its dissipation rate or the equivalent turbulent length scale [22–25]. These models postulate a turbulent viscosity, a Reynolds stress, and dissipation terms, as well as a buoyancy term for modeling RT and RM instabilities. They are able to handle multi-dimensions, multi-fluids, and variable accelerations, however, they too cannot address de-mixing (at least in their present form). A more advanced version of the single fluid approach is the BHR (Besnard-Harlow-Rauenzahn) turbulent-mix model [26]. Evolution equations from second-order correlations were developed and gradient-diffusion approximations were applied to close the system of equations [26]. Using a mass weighted averaged decomposition, the original BHR model included full transport equations for Reynolds stress tensor, turbulent mass flux, density fluctuations and the dissipation rate of the turbulent kinetic energy. A reduced, simpler but still accurate, version of the model has been previously presented [27, 28], showing very promising results.

Despite the aforementioned efforts, there is still uncertainty about the optimum choice of engineering turbulence models for flows involving RT (and RM) mixing, as well as lack of comparisons between different models. Many of the flows are highly compressible. However, turbulent velocity fluctuations are usually small compared to the speed of sound. Hence it is essential that the models give good results for low-Mach number RT mixing. The problem considered in the paper is the simplest such case in which the fluid densities and acceleration remain constant and self-similar mixing occurs. This and other near-incompressible self-

similar test cases have been widely used by other researchers, [22] for example, as the starting point for the development of models for RT/RM mixing. In the RT test case the depth, at time t, to which the turbulent mixing zone extends into to denser fluid 1 is given by:

$$h_1 = \alpha \frac{\rho_1 - \rho_2}{\rho_1 + \rho_2} g t^2 \tag{1}$$

where ρ_1 and ρ_2 are the densities of the two fluids, g is the acceleration and α is a constant for self-similar mixing. Two different density ratios are considered ρ_1/ρ_2=3 and 20. For RT experiments $\alpha \sim 0.05$ to 0.06. However, when simulations (ILES or DNS) are performed using ideal initial conditions (small random short wavelength perturbations) much lower values of $\alpha \sim 0.026$ are obtained [6, 9]. The higher observed values of α are attributed to the influence of the initial conditions. This presents a problem for turbulence modelling. All the turbulence models referred to herein will, when model coefficients are specified, give a unique value of α (at least for a given density ratio). It is argued here that the turbulence model coefficients should, for practical purposes, be chosen to match a typical experimental value of α. The value chosen in this paper is α=0.06. For the ILES described in [9], long wavelength random perturbations where included in the simulations to approximate self-similar mixing at the higher observed values of α.

The aim of this work is twofold:

- To propose specific modifications to the original *K-L* model of Dimonte and Tipton [22], which lead to significant improvements in the modeling predictions; for simplicity the modified model will be henceforth labeled throughout the paper as the *K-L* model;

- To compare the *K-L* and Youngs' multi-fluid model in 1D Rayleigh-Taylor mixing flows.

The present study provides an initial step towards a systematic comparison and a better understanding of single (two-equation) and multi-fluid models. Comparisons with 3D simulations for more complex flows are considered essential for assessing the advantages of the more advanced RANS models such as multi-fluid or BHR over the relatively simple single-fluid models.

II. TURBULENCE MODELS

A. Youngs' multi-fluid model

The turbulent mixing model is implemented for many fluids in a two-dimensional compressible Eulerian hydro-code [19]. However, all the calculations shown here are for mixing of two fluids (henceforth labeled as TF) in one dimension at a sufficiently low Mach number to give incompressible behavior. Hence, for simplicity, the incompressible limit of the model equations for one dimensional two-fluid mixing is given here. The volume fractions for the two "phases" are denoted by f_r $(r = 1, 2)$. Initially, these correspond to the two initial fluids which have densities ρ_r^0 $(r = 1, 2)$. As the fluids mix, mass is exchanged between the two phases and this is used to represent the molecular mixing process [29], i.e., the random mixture of the two fluids is represented by two phases, one rich in initial fluid 1 and one rich in initial fluid 2. Phase r consists of fractions α_{rs} by volume of fluid s. Hence the density of phase r is $\rho_r = \alpha_{r1}\rho_1^0 + \alpha_{r2}\rho_2^0$ and the mean density of the mixture is $\rho = f_1\rho_1 + f_2\rho_2$. The equations for the volume fractions f_r and α_{rs} are:

$$\frac{\partial f_r}{\partial t} + \frac{\partial}{\partial x}\{f_r\bar{u}_r\} = \Delta V_{r'r} - \Delta V_{rr'} \tag{2}$$

$$\frac{\partial f_r\alpha_{rs}}{\partial t} + \frac{\partial}{\partial x}\{f_r\alpha_{rs}\bar{u}_r\} = \frac{\partial}{\partial x}\left(f_r D \frac{\partial\alpha_{rs}}{\partial x}\right) + \tag{3}$$
$$\alpha_{r's}\Delta V_{r'r} - \alpha_{rs'}\Delta V_{rr'}$$

In equations (2) and (3) $\bar{u}_r$ denotes the *volume-weighted* mean velocity for phase r. For the one dimensional problems considered here the volume weighted mean velocity for the mixture is zero, i.e. $f_1\bar{u}_1 + f_2\bar{u}_2 = 0$. ΔV_{rs} is the rate at which the volume is transferred from phase r to phase s and phase r' denotes the phase which is not phase r. D is the turbulent diffusivity.

Mass-weighted mean phase velocities, u_r, are needed for the momentum equations. Both $\bar{u}_r$ and u_r include the effects of mixing due to turbulent diffusion and their difference is attributed to within-phase turbulent diffusion and is prescribed as follows [19]:

$$u_r - \bar{u}_r = u_r^d - \bar{u}_r^d \tag{4}$$

5

where

$$u_r^d = -\frac{D}{\rho_r f_r} \frac{\partial (\rho_r f_r)}{\partial x}$$

and

$$\bar{u}_r^d = -\frac{D}{f_r} \frac{\partial f_r}{\partial x}$$

Momentum equations are solved for mass-weighted mean phase velocities, u_r:

$$\frac{\partial f_r \rho_r u_r}{\partial t} + \frac{\partial f_r \rho_r u_r^2}{\partial x} = -f_r \frac{\partial P}{\partial x} + F_r \frac{\partial \tau_{xx}}{\partial x} + X_{rr'} + f_r \rho_r g \tag{5}$$

In equation (5), P denotes the common pressure, F_r is the phase r mass fraction, τ_{xx} is the Reynolds' stress component and $X_{rr'} = -X_{r'r}$ is the momentum exchange between the two phases. The momentum exchange consists of drag (C-term), added mass (A-term) and mass exchange effects:

$$
\begin{aligned}
X_{rr'} &= C\left(u_{r'} - u_r - u_{r'}^d + u_r^d\right) \\
&+ A\left(\frac{D_{r'}u_{r'}}{Dt} - \frac{D_r u_r}{Dt}\right) + \Delta U_{rr'}
\end{aligned}
\tag{6}
$$

where

$$\frac{Du_r}{Dt} = \frac{\partial u_r}{\partial t} + u_r \frac{\partial u_r}{\partial t}$$

If turbulent diffusion effects are absent, the mass exchange term is:

$$
\begin{aligned}
\Delta U_{rr'} &= \Delta M_{r'r} u_{r'} - \Delta M_{rr'} u_r = \Delta M \left(u_{r'} - u_r\right) + \\
&\quad \left(F_{r'} u_r + F_r u_{r'}\right)\left(\Delta M_{r'r} - \Delta M_{rr'}\right)
\end{aligned}
\tag{7}
$$

where $\Delta M_{rs} = \rho_r \Delta V_{rs}$ and $\Delta M = F_{r'} M_{r'r} + F_r M_{rr'}$.

When turbulent diffusion effects are included the term involving ΔM is replaced by $\Delta M \left(u_{r'} - u_r - u_{r'}^d + u_r^d\right)$. This ensures that if either $C \to \infty$ or $\Delta M \to \infty$ then mixing is purely diffusive.

Two further equations, for turbulent kinetic energy, K, and length scale L, are used to close various terms in equations (2) to (6). These are:

$$\frac{\partial (\rho K)}{\partial t} + \frac{\partial (\rho K u)}{\partial x} = \frac{\partial}{\partial x}\left(\rho D_K \frac{\partial K}{\partial x}\right) + S_K - \rho \epsilon \tag{8}$$

$$\frac{\partial (L)}{\partial t} + u_L \frac{\partial L}{\partial x} = \frac{\partial}{\partial x}\left(D_L \frac{\partial L}{\partial x}\right) + S_L \tag{9}$$

6

where D_K, D_L are the turbulent diffusion coefficients and $S_K = (u_2 - u_1) X_{12}$, S_L are the source terms. The turbulence dissipation rate is ϵ and $u = F_1 u_1 + F_2 u_2$. In the equation for L, u_L denotes the advection velocity. The advective term $u_L dL/dx$ spreads out the length scale to fill the mixing zone without increasing or decreasing L. This is considered physically reasonable and is chosen in preference of a conservative term.

The full compressible version of the model includes internal energy equations for each fluid, as described in [19]. The model is able to represent the mixing of several fluids and results for compressible flow (a simplified implosion) and three-fluid mixing are given in [30].

The two-fluid approach may be regarded as a model for the dynamics of the large-scale structures present in the mixing zone (parcels of heavy fluid and parcels of light fluid) and has much in common with two-phase flow models for gas-particle mixtures. Processes such as differential acceleration by shock or pressure gradient, drag, added mass, are modeled in a physically plausible way. It is argued that this gives the correct dynamical behavior for a range of complex flows. The way the present model is constructed is very different to that generally used for RANS models, which is based on the closure of fluctuating quantities. However, it should be noted that Llor [21] does provide a statistical derivation of the two-fluid model. Assessment of the merits and weaknesses of these two approaches is a key aspect of the current and forthcoming papers.

1. Closure Approximations

A number of the terms appearing in equations (2) to (9) require closure approximations. These are given below:

$$C = c_1 \frac{\rho f_1 f_2}{L} \left| u_1 - u_2 - u_2^d + u_1^d \right| \tag{10}$$

$$\tau_{xx} = \frac{2}{3} \rho K - \frac{4}{3} \mu_t \frac{\partial u}{\partial x} \tag{11}$$

where $\mu_t = \rho \sqrt{K} \ell_t$ and $\ell_t = c_2 L$.

$$\Delta V_{12} = f_2 \dot{V}, \ \Delta V_{21} = f_1 \dot{V} \tag{12}$$

where entrainment rate ($\dot{V}$) is given by

$$\dot{V} = c_3 f_1 f_2 \frac{\sqrt{K}}{\ell_t}$$

and turbulent dissipation rate (ϵ)

$$\epsilon = c_4 \frac{K^{3/2}}{\ell_t}$$

Four model constants have been introduced, c_1, c_2, c_3, c_4, which need to be chosen by the calibration process. Other terms in the model use typical values and are not varied: $D = 2\sqrt{K}\ell_t$, $D_K = D_L = 4\sqrt{K}\ell_t$. The added mass term uses the added mass coefficient of $1/2$ for a solid sphere: $A = \rho f_1 f_2 / 2$.

Finally, the closure of the length scale equation needs to be described. The source term uses a velocity difference in the direction of mixing to give L proportional to the mixing zone width. When mass exchange between the initial fluids is included, the phase velocity difference, $u_1 - u_2$, only accounts for some of the mixing as it does not allow for within-phase diffusion. It proves necessary to re-construct *fluid* velocities, $\hat{u}_s$. The initial fluid s volume fraction is given by $\hat{f}_s = f_1\alpha_{1s} + f_2\alpha_{2s}$ and the equation for $\hat{u}_s$ is obtained by summing (3) for $r =1$ and 2 using (4):

$$\frac{\partial \hat{f}_s}{\partial t} + \frac{\partial \hat{f}_s \hat{u}_s}{\partial x} = 0 \tag{13}$$

with

$$\hat{f}_s \hat{u}_s = f_1\alpha_{1s}\left(u_1 - u_1^d\right) + f_2\alpha_{2s}\left(u_2 - u_2^d\right) - D\frac{\partial \hat{f}_s}{\partial x}$$

The advection velocity and source terms in the length scale equation are now defined as $u_L = \hat{f}_2\hat{u}_1 + \hat{f}_1\hat{u}_2$ and

$$S_L = \left(\frac{2\rho}{\rho_1^0 + \rho_2^0}\right)^p (\hat{u}_1 - \hat{u}_2) \tag{14}$$

The form of u_L is chosen to transport the length scale to the edges of the mixing zone - if $\hat{f}_1 = 0$ (spike tip) then $u_L = \hat{u}_1$ (spike tip velocity). The density factor in the source term is used to reduce the length scale on the low-density side of the mixing zone and give the required spike/bubble asymmetry. One more model constant p, is introduced here.

2. Model Constants

The key test problem used for mix model calibration is self-similar RT mixing for which the bubble distance, the depth to which the instability penetrates the denser fluid, is given by $h_b = \alpha A g t^2$, where A is the Atwood number. Model constants are chosen here to give $\alpha = 0.06$ and the overall degree of molecular mixing and fraction of turbulence dissipated

ρ_1/ρ_2	3:1	20:1
c_1	4.062	3.765
c_2	0.13	0.13
c_3	0.2321	0.2039
c_4	0.1984	0.2228
p	0.3802	0.3802

TABLE I: Two-fluid model constants.

indicated by ILES results [9]. The exponent p is chosen to give the required spike/bubble asymmetry at $\rho_1/\rho_2 = 20$. Hence c_1, c_3, c_4 and p are specified. The model coefficient c_2 determines the relative importance of diffusive mixing and pressure gradient driven mixing. The one-dimensional test cases considered here can be modeled equally well with different proportions of diffusive mixing. When c_2 is varied, the remaining constants are re-adjusted to give the same growth rate, degree of molecular mixing etc. The best choice for c_2 needs to be found by considering a wider range of test problems. The value used here gives $\sim 45\%$ of mixing due to turbulent diffusion.

The model coefficients used in the full version of the model are in general functions of α and A and for a given application the coefficient set for a suitable value of α is chosen. However, in this paper only two values of A are required with α=0.06, which are shown in Table I.

B. *K-L* multi-component turbulence model

The *K-L* model was previously proposed by Dimonte and Tipton [22] for describing the turbulent self-similar regime of Rayleigh-Taylor and Richtmyer-Meshkov mixing. The starting point for deriving the model equations are the buoyancy-drag models for the self-similar growth of RT and RM instabilities [13, 15]. In the present work, a modified version of the *K-L* is proposed. The modifications, which are presented in detail below, concern: i) the model formulation in terms of the total energy instead of the internal energy; ii) the implementation of the source term in the turbulent kinetic energy equation; iii) the turbulent diffusion of enthalpy instead of the internal energy; and iv) the calculation of the local Atwood number based on a higher-order numerical approximation.

9

Note that the total energy equation (18) uses the diffusion of internal energy as was originally formulated [22]. The proposed modification to change the diffusion of internal energy to enthalpy is detailed in section II D.

1.   Governing equations

The mean flow is described by the Favre-averaged conservation equations for the mass, momentum and energy of the mixture, and for the mass fractions of the components:

$$\frac{\partial \bar{\rho}}{\partial t} + \frac{\partial}{\partial x_i}(\bar{\rho}\tilde{u}_i) = 0 \tag{15}$$

$$\frac{\partial}{\partial t}(\bar{\rho}\tilde{u}_i) + \frac{\partial}{\partial x_j}(\bar{\rho}\tilde{u}_i\tilde{u}_j) = -\frac{\partial \bar{p}}{\partial x_i} - \frac{\partial \tau_{ij}}{\partial x_j} + \bar{\rho}g \tag{16}$$

$$\begin{aligned}
\frac{\partial}{\partial t}(\bar{\rho}E^*) + \frac{\partial}{\partial x_i}(\bar{\rho}E^*\tilde{u}_i) &= -\frac{\partial}{\partial x_i}(\bar{p}\tilde{u}_i) - \frac{\partial \tau_{ij}\tilde{u}_j}{\partial x_i} \\
&+ \frac{\partial}{\partial x_i}\left(\frac{\mu_t}{N_e}\frac{\partial \tilde{e}}{\partial x_i}\right) + \frac{\partial}{\partial x_i}\left(\frac{\mu_t}{N_K}\frac{\partial K}{\partial x_i}\right) + \bar{\rho}\tilde{u}_i g
\end{aligned} \tag{17}$$

$$\frac{\partial}{\partial t}(\bar{\rho}\tilde{F}) + \frac{\partial}{\partial x_i}(\bar{\rho}\tilde{F}\tilde{u}_i) = \frac{\partial}{\partial x_i}\left(\frac{\mu_t}{N_F}\frac{\partial \tilde{F}}{\partial x_i}\right) \tag{18}$$

where g is the gravitational acceleration. For a 1-Dimensional ($1D$) flow $i = j = 1$.

In the above equations, the statistical (Reynolds) average of a quantity ϕ is denoted by $\bar{\phi}$ and its corresponding fluctuation by ϕ'. The Favre average $\tilde{\phi}$ is defined by $\tilde{\phi} = \overline{\rho\phi}/\bar{\rho}$ and its corresponding fluctuation by ϕ''. $\tilde{F}$ is the mass fraction, and for perfect gases $\bar{p} = \bar{\rho}R\tilde{T}$, where R is the gas constant and $\tilde{T}$ is the Favre average static temperature corresponding to the static pressure. The modified total energy is defined by:

$$E^* = \tilde{e} + \frac{\tilde{u}_k\tilde{u}_k}{2} + K \tag{19}$$

where $\tilde{e}$ is the internal energy per unit mass; note that E^* is not equal to the Favre average of E. The viscous stresses and the heat conduction were neglected.

The eddy viscosity is calculated using the usual relation for the two equations eddy viscosity models:

$$\mu_t = C_\mu \bar{\rho} u_t L \tag{20}$$

where C_μ is a model constant (Table II) and $u_t = \sqrt{2K}$ is the turbulent velocity.

With regard to the turbulent stresses, it is recommended [22, 31] that in the presence of strong shocks the deviatoric part of this tensor should be omitted and the turbulence stresses should be approximated by the turbulence pressure:

$$\tau_{ij} = \delta_{ij} C_P \bar{\rho} K \tag{21}$$

where C_P is a free parameter of the model, which is generally taken as 2/3 (Table II) and δ_{ij} is the Kronecker delta. Dimonte and Tipton [22] mentioned that if the deviatoric part of the turbulent shear stress tensor is not ommited, then the strain rates become unphysically large; see also [23, 32]. The same conclusion was also drawn in the course of our research both for the original and the modified K-L model.Furthermore, since the *K-L* mixing model is currently constituted without any turbulent shear stress components, it cannot describe the Kelvin-Helmholtz (KH) instability. Though this problem is found in many mixing models, it could be ameliorated in the future by the inclusion of a self-limited (realizable) turbulent shear stress. Despite this, symmetric ICF implosions do not tend to form KH type instabilities and are thus not important in such flows, though they can still occur in asymmetric implosions.

The turbulent diffusion terms are adjusted using dimensionless scaling factors, such that N_e (or N_h) and N_F correspond to the turbulent Prandtl and Schmidt numbers (model constants) respectively.

2. Model equations

The transport equation for the turbulent kinetic energy (TKE) denoted as K is:

$$\begin{aligned}
\frac{\partial}{\partial t}(\bar{\rho}K) + \frac{\partial}{\partial x_i}(\bar{\rho}K\tilde{u}_i) &= -\tau_{ij}\frac{\partial \tilde{u}_i}{\partial x_j} \\
&+ \frac{\partial}{\partial x_i}\left(\frac{\mu_t}{N_K}\frac{\partial K}{\partial x_i}\right) + S_K - \bar{\rho}\epsilon
\end{aligned} \tag{22}$$

N_K is the diffusion coefficient for the turbulent kinetic energy K.

The implementation of the source term S_K is defined according to the time scales of the mean flow, Θ, and turbulent structures, Θ_t as:

$$\Theta = \bar{\rho}\left(\gamma\frac{\bar{p}}{\bar{\rho}}\right)^{1/2}\left(\frac{\partial \bar{p}}{\partial x_k}\frac{\partial \bar{p}}{\partial x_k}\right)^{-1/2} \tag{23}$$

$$\Theta_t = \frac{L}{\sqrt{K}} \tag{24}$$

If the time scale of the mean flow is much smaller than the turbulent time scale, the instability is considered to be *impulsive* (RM-like), otherwise *gradual* (RT-like):

$$S_K = \begin{cases} C_B \bar{\rho} u_t \left| A_{\mathrm{L}i} g_i \right| & \text{if } \Theta < \Lambda_\Theta \Theta_t \\ \\ C_B \bar{\rho} u_t \max\left(0, \ A_{\mathrm{L}i} g_i\right) & \text{otherwise} \end{cases} \tag{25}$$

where $\Lambda_\Theta \leq 1$ is a coefficient. In the present study, $\Lambda_\Theta = 1$ was used throughout the calculations. This criterion is based on the sudden acceleration of a fluid particle (estimated by the pressure gradient) and is not directly dependent on the CFL number. In (25), $g_i = -(1/\bar{\rho})\partial\bar{p}/\partial x_i$ is the acceleration and $A_{\mathrm{L}i}$ is the local Atwood number.

The dissipation of the turbulent kinetic energy, ϵ, represents the mechanical work of the drag forces on the turbulent structures (bubbles and spikes):

$$\epsilon = C_D \frac{u_t^3}{L} \tag{26}$$

where C_D is the drag coefficient (Table II).

The presentation of the model is completed by the equation for the turbulent (or eddy) length scale, L:

$$\begin{aligned}
\frac{\partial}{\partial t}(\bar{\rho}L) + \frac{\partial}{\partial x_i}(\bar{\rho}L\tilde{u}_i) &= \frac{\partial}{\partial x_i}\left(\frac{\mu_t}{N_L}\frac{\partial L}{\partial x_i}\right) \\
&+ C_L \rho u_t + C_C \rho L \frac{\partial \tilde{u}_i}{\partial x_i}
\end{aligned} \tag{27}$$

where the production is given by $C_L \rho u_t$; the last term models the compressibility effects; and C_L, C_C and N_L are model constants (Table II).

Finally, using the isobaric assumption for the thermodynamic closure of the mixture [33], the heat capacity ratio γ is given by:

$$\gamma = 1 + \frac{1}{\frac{f_1}{\gamma_1 - 1} + \frac{f_2}{\gamma_2 - 1}} \tag{28}$$

where f_1 and f_2 are the volume fractions of components 1 and 2. The volume fraction is calculated by the mass fraction using the following relationship:

$$f_1 = \frac{F_1/M_1}{F_1/M_1 + F_2/M_2} \tag{29}$$

where M_i is the molar mass of species i and obviously $f_1 + f_2 = 1$.

12

ρ_1/ρ_2	3:1	20:1
Eddy viscosity (C_μ)	0.70	0.68
Turbulent pressure (C_P)	0.667	0.667
Eddy size production (C_L)	1	1
Eddy compression (C_C)	0.333	0.333
Local Atwood number (C_A)	2	2
Drag (C_D)	0.92	0.90
Buoyancy (C_B)	0.86	0.97
Diffusion L (N_L)	0.125	0.125
Diffusion e (N_e)	1.125	1.125
Diffusion h (N_h)	1.125	1.125
Diffusion F (N_F)	1.125	1.125
Diffusion K (N_K)	1.5	1.5

TABLE II: The K-L model coefficients.

3. K-L model coefficients

The values of the constant coefficients for the modified K-L model here are different than the original K-L model of Dimonte and Tipton [22]. The values of C_μ, C_D and C_B are chosen to give the best possible overall results for the key terms examined (temporal evolution of total-Mix and K_{max}, and spatial profiles of VF and K/K_{max}).

Dimonte and Tipton [22] derived the model coefficients based on a number of approximations. The coefficients were derived for $A_0 \ll 1$ or $A_0 \approx 0$ by neglecting density gradient terms. They also mentioned that "*analytical solutions to the model equations are not yet available for $A_0 \sim 1$*". Furthermore, for high Atwood numbers the ratio of the turbulent kinetic energy (KE) to potential energy (PE) does not remain constant, i.e., KE/PE $< 1/2$, but decreases, as experimental observations suggest, to a value of KE/PE ≈ 0.3 for $A_0 \sim 1$, thus yielding $N_K > 2N_L$. Dimonte and Tipton [22] also showed that decreasing the value of N_L, the volume fraction (VF) profiles sharpen. Due to the different numerical frameworks used in [22] and here, the model constants require some re-adjustment. As the effect of the numerical dissipation is to enhance diffusion [34], e.g., widen the VF profiles, it is

expected that the diffusion constant N_L will require a smaller value than the one suggested analytically. Numerical simulations showed that $N_K = 9N_L$, which agrees with the finding of $N_K > 2N_L$ [22] for Atwood numbers greater than zero. Similar to [22], in the present paper $N_K = N_F = N_e = 1 \pm 0.2$.

In [22] the model coefficients were derived analytically for self-similar solutions and under the assumptions of: a) simple flows in the incompressible limit with nearly constant density, $A_0 \to 0$; and b) maximum values of the L and K in the self-similar profiles occurring at the interface and vanishing symmetrically at the mixing boundary. The simplest form that describes the above conditions is given by:

$$K\left(x,t\right) = K_0(t)\left(1 - \frac{x^2}{h^2(t)}\right)$$

$$L\left(x,t\right) = L_0(t)\sqrt{1 - \frac{x^2}{h^2(t)}} \tag{30}$$

These functions are also used to replace the turbulent length scale L and turbulent kinetic energy K in the governing equations (for terms such as $\mathrm{D}L/\mathrm{D}t$, $\mathrm{d}L/\mathrm{d}x$ etc) in order to obtain the analytical self-similar expressions.

In [22] the K-L model is calibrated to be able to describe the observation [19, 35, 36] that 50% of the potential energy is converted into turbulent kinetic energy, while the other half is dissipated, so the ratio of the turbulent kinetic energy to potential energy $\mathrm{KE}/\mathrm{PE} \approx 0.5$. However, this value holds true only when the initial Atwood number is $A_0 \approx 0$. Assuming that $A_0 \to 1$, [36] gives a value of $\mathrm{KE}/\mathrm{PE} \sim 0.3$. It was also shown [22] that

$$\beta = \sqrt{\frac{N_L}{2C_\mu}} \tag{31}$$

where $\beta \equiv L_0/h$ is the self-similarity ratio and

$$\frac{KE}{PE} \sim 32\beta^2\alpha_b \sim 16\frac{N_L}{C_\mu}\alpha_b \tag{32}$$

In the present work, $\alpha_b = 0.06$ is used to match experimental observations. Using $\mathrm{KE}/\mathrm{PE} \sim 0.3$, for large Atwood numbers, and $C_\mu \equiv 0.7$, the turbulent length scale diffusion coefficient is now equal to $N_L \approx 0.21875$.

Assuming $A_0 \ll 1$, Dimonte and Tipton [22] showed that

$$\frac{\partial L_0}{\partial t} \sim \frac{V_0}{2} \tag{33}$$

14

where $V_0 = \sqrt{2K_0}$. Assuming $A_0 \gg 0$, the full self-similar form of the L equation can be obtained [22]:

$$\frac{\partial L_0}{\partial t} \sim \frac{V_0}{2} \left[1 - A_0 \chi \left(1 - \chi^2 \right) \right] , \tag{34}$$

where $\chi = x/h$ is the scaled distance (x is the spatial location and $h(t)$ is the bubble height at time t). The correction term in the brackets has a maximum value of $3A_0/8$ when $\chi = 0.5$. According to [22], N_F can be obtained by the expression, which is derived by the mass fraction equation:

$$\frac{1}{2L_0} \frac{\partial L_0}{\partial t} \sim \frac{C_\mu}{N_F} \beta \frac{V_0}{h} \tag{35}$$

which leads to $N_F = 2N_L$ assuming $A_0 \ll 1$ and using (33). However, at the high Atwood number limit $A_0 \to 1$ one can use (34) to substitute dL_0/dt in (35), thus at the maximum scaled distance of $\chi = 0.5$,

$$N_F \sim \frac{16}{8 - 3A_0} N_L \sim 3.2 N_L \tag{36}$$

This value indicates that for large Atwood numbers, the value of N_L should be at least 3 times smaller than N_F. The above analysis suggests that the constants used in the present study are consistent with those derived by Dimonte and Tipton [22] for low Atwood number flows. Therefore, $N_F > 2N_L$ and $N_L < 0.5$ for $A_0 > 0$. The remainder of the constants are either equal to or satisfy the relations/conditions proposed in [22].

4. Local Atwood number estimation

The local Atwood number (A_{Li}) used in source term S_K is defined by [22]:

$$A_{\mathrm{L}i} = A_{0i} + A_{\mathrm{SS}i} \tag{37}$$

A_{0i} recovers the initial Atwood number at the interfaces between fluids, where the density is discontinuous and $A_{\mathrm{SS}i}$ represents the local Atwood number in the self-similar regime, where the density variation is gradual.

The initial cell Atwood number (A_{0i}) can be expressed in terms of the reconstructed values of the densities at the cell's faces as:

$$A_{0i} = \max \left(A_{0i-\frac{1}{2}}, A_{0i+\frac{1}{2}} \right) \tag{38}$$

and the cell face Atwood number ($A_{0i\pm1/2}$) can be calculated using reconstructed values of the density at the cell faces.

$$A_{0i-\frac{1}{2}} = \frac{\bar{\rho}_{L+} - \bar{\rho}_{L-}}{\bar{\rho}_{L+} + \bar{\rho}_{L-}}, \quad A_{0i+\frac{1}{2}} = \frac{\bar{\rho}_{R+} - \bar{\rho}_{R-}}{\bar{\rho}_{R+} + \bar{\rho}_{R-}} \tag{39}$$

where the subscripts L and R stand for the left and right faces of the cell, respectively. In the general three-dimensional case, the computational cells are assumed hexahedral with the faces perpendicular to the spatial directions. The reconstructed density values were recommended [22] to be obtained using van Leer's monotonicity principle [37] such that:

$$
\begin{aligned}
\bar{\rho}_{L+} &= \bar{\rho}_i - \frac{\Delta x}{2} \left(\frac{\partial \bar{\rho}}{\partial x}\right)_i^{\text{MON}} \\
\bar{\rho}_{L-} &= \bar{\rho}_{i-1} - \frac{\Delta x}{2} \left(\frac{\partial \bar{\rho}}{\partial x}\right)_{i-1}^{\text{MON}}
\end{aligned}
\tag{40}
$$

and

$$\left(\frac{\partial \bar{\rho}}{\partial x}\right)_i^{\text{MON}} = \text{sign}\left(\Delta\bar{\rho}_{i+1}\right) \min\left(\frac{|\Delta\bar{\rho}_{i+1}|}{\Delta x}, \frac{\Delta\bar{\rho}_i}{\Delta x}\right) \tag{41}$$

where $\Delta\bar{\rho}_i = (\bar{\rho}_i - \bar{\rho}_{i-1})$.

The self-similar cell Atwood number (A_{SSi}) is given by:

$$A_{\text{SS}i} = C_A \frac{L}{\bar{\rho} + L \left|\frac{\partial \bar{\rho}}{\partial x}\right|_i^{\text{MON}}} \left(\frac{\partial \bar{\rho}}{\partial x}\right)_i^{\text{MON}} \tag{42}$$

where C_A is a model constant (Table II). A simplified formula for calculating the self-similar Atwood number, $A_{\text{SS}i}$, was employed [38]:

$$A_{\text{SS}i} = \frac{L}{\bar{\rho}} \left(\frac{\partial \bar{\rho}}{\partial x}\right)_i^{\text{MON}} \tag{43}$$

Here, we propose to calculate the densities at the cell face by simple averaging of the numerically reconstructed values, which are obtained from the calculation of the inviscid fluxes (Figure 1), instead of using equation (40). Thus, the densities used in (38) are calculated by:

$$
\begin{aligned}
\bar{\rho}_{\text{R}} &= \frac{1}{2}\left(\bar{\rho}_{\text{R-}} + \bar{\rho}_{\text{R+}}\right) \\
\bar{\rho}_{\text{L}} &= \frac{1}{2}\left(\bar{\rho}_{\text{L-}} + \bar{\rho}_{\text{L+}}\right)
\end{aligned}
\tag{44}
$$

16
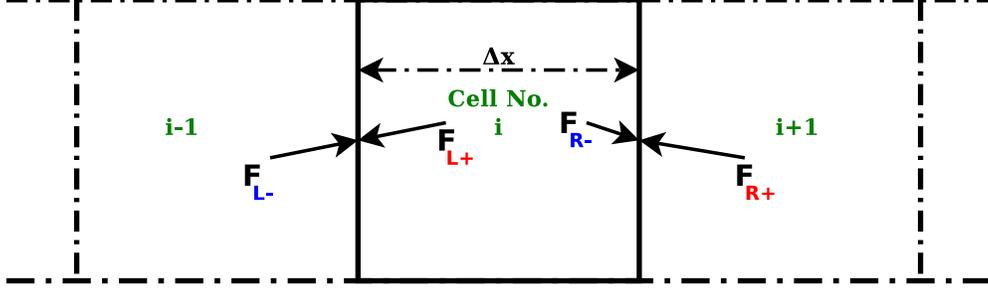
FIG. 1: Location of variables used to obtain cell center spatial derivatives.

and the cell-center density gradient used for the self-similar Atwood number (A_{SSi}) in equation (42) is calculated by a first-order central difference:

$$\frac{\partial \bar{\rho}}{\partial x} = \frac{\bar{\rho}_{\mathrm{R}} - \bar{\rho}_{\mathrm{L}}}{\Delta x} \tag{45}$$

The cell initial Atwood number (A_{0i}) is then calculated as:

$$A_{0i} = \frac{\bar{\rho}_{\mathrm{R}} - \bar{\rho}_{\mathrm{L}}}{\bar{\rho}_{\mathrm{R}} + \bar{\rho}_{\mathrm{L}}} \tag{46}$$

It was found that using equation (37) for the calculation of the local Atwood number in the turbulent kinetic energy production source term S_K (equation (22)), over-predicts the initial growth rate; this is due to the large A_{0i}, as well as the additional A_{SSi} term. To overcome this problem, equation (37) is reformulated by using a weighted sum of both the initial and self-similar Atwood number terms, which depends on the value of the turbulent length scale (L) to cell-width (Δx) ratio:

$$A_{\mathrm{L}i} = (1 - w_L) A_{0i} + w_L A_{\mathrm{SS}i} \tag{47}$$

where the weighting factor $w_l = \min\left(L/\Delta x, 1\right)$ is the ratio of the turbulent mixing length L to the grid cell size Δx. This ensures that when L becomes sufficiently large, the Atwood number is solely based on $A_{\mathrm{SS}i}$, while initially is dominated by A_{0i}.

C. Numerical implementation of turbulence models

1. Two-Fluid model

The TF model has been numerically implemented using the Lagrange-Remap method [18, 19]. The volume fractions, densities, internal energies and turbulent kinetic energy are

17

defined at cell centers, while the velocity components and length scale are defined at the vertices. The calculation for each time step is divided into a mixing phase, a Lagrangian phase and a remap phase. In the mixing phase the fluxes due to the velocity difference, $\mathbf{u}_r - \bar{\mathbf{u}}$, are calculated. In the Lagrangian phase, the changes in multi-fluid velocities and internal energies due to pressure terms are calculated using a second-order-accurate time-integration technique. The fluxes across the cell faces due to the velocity $\bar{\mathbf{u}}$ are calculated in the remap phase. The spatial discretisation in the remap is obtained by the third-order-accurate, monotonic advection scheme [37]. As all the variables in the remap phase are passively advected, numerical mixing can be minimized, compared to the schemes typical in finite volume codes, by allowing the reconstructed slope to depend on the advection timestep. Most of the computational steps use explicit time integration; little iteration is needed (unless complex equations of state are used for mixtures). Althought it appears more difficult to implement the TF model than the *K-L* model, it is argued here that use of suitable operator splitting in the Lagrange-remap method makes this a relatively straightforward process, which does not increase computer time requirements by a large factor.

The ILES results used in the assessment of the turbulence models have also been obtained using the Lagrange-Remap method, but with a single velocity field. Further details on the ILES method can be found in the literature [19, 39].

2. *K-L model*

The *K-L* model has been numerically implemented for the compressible Euler equations (molecular effects assumed negligible) using the finite volume Godunov-type [40] (upwind) method. Additionally, the following is used: 1) the isobaric assumption to estimate the heat capacity ratio of the mixture equation (28); 2) the MUSCL 5th-order [41] augmented by a low Mach number correction [42] for reconstructing the variables $[\rho(1 - F), \rho u, p, \rho F, \rho K, \rho L]$; 3) the HLLC solver [43] along with the pressure-based wave speed estimate (PVRS) method for the solution of the numerical inter-cell flux estimation (Riemann problem); and 4) a third order TVD Runge-Kutta scheme for time integration; see [44–47] and references therein. It has been found that the above procedure does not generate any unphysical pressure oscillations at the interface between components of different heat capacity ratios ($\gamma_1 \neq \gamma_2$).

D. Enthalpy diffusion

It has been suggested [48] that when there is species diffusion between N different fluids in multi-component flows (whether turbulent or molecular), an enthalpy diffusion term should be present to account for the energy transfers associated with the compositional changes. The term referred to as the inter-diffusional enthalpy flux is given by:

$$q_d = \sum_{i=1}^{N} \bar{J}_i \tilde{h}_i \tag{48}$$

The diffusion of enthalpy is a well known process in the reacting flow community, where changes in temperature and composition are ubiquitous [49]. For turbulent diffusion it is reasonable to assume that the diffusivities are the same for all fluid species. The relative mass fluxes, $\bar{J}_i$, are then given by:

$$\bar{J}_i = -\bar{\rho} D \frac{\partial \tilde{F}_i}{\partial x} \tag{49}$$

where

$$\bar{\rho} D = \frac{\mu_t}{N_F} \tag{50}$$

and $\tilde{h}_i$ is the specific enthalpy of species (i)

$$\tilde{h}_i = \tilde{e}_i + \frac{\bar{p}_i}{\bar{\rho}_i} = \gamma_i \tilde{e}_i \tag{51}$$

and for the mixture

$$\tilde{h} = \sum_{i=1}^{N} \left(\tilde{F}_i \tilde{h}_i \right) \tag{52}$$

There is also an energy flux due to heat conduction:

$$q_c = \bar{\rho} D_{th} c_v \gamma \frac{\partial \tilde{T}}{\partial x} \tag{53}$$

where D_{th} is, in the present case, the turbulent thermal diffusivity and $\tilde{T}$ is the temperature of the mixture. The mult-fluid model uses a different treatment for the flow of energy in which separate equations are used for the internal energies of each phase [19]. The TF model does not use (48) but it will be shown here that equivalent results are obtained for the RT test case.

In this paper, compressible models are used at low Mach number to simulate incompressible mixing. Hence, it is important to consider the incompressible limit of the compressible

model. Other researchers [50] have pointed out that when diffusivity is present, the mass-weighted mean velocity, $\tilde{u}$, is no longer divergence free in the incompressible limit. For perfect gases with different molecular properties but with equal temperature and pressure at the interface, the incompressible limit ($t \to \infty$) gives [50]:

$$\frac{\partial}{\partial x}\left(\tilde{u} + \frac{D}{\bar{\rho}}\frac{\partial \bar{\rho}}{\partial x}\right) = 0 \tag{54}$$

and (15) now becomes

$$\frac{\partial \bar{\rho}}{\partial t} = \frac{\partial}{\partial x}\left(D\frac{\partial \bar{\rho}}{\partial x}\right) \tag{55}$$

Rayleigh-Taylor mixing can also occur at the boundary between two regions of the same fluid at the same pressure but at different temperatures. In the incompressible limit ($p \to \infty$), eqn.(15) takes the form:

$$\frac{\partial \bar{\rho}}{\partial t} = \frac{\partial}{\partial x}\left(D_{th}\frac{\partial \bar{\rho}}{\partial x}\right) \tag{56}$$

For high-Reynolds number Rayleigh-Taylor mixing these two cases are equivalent in the incompressible limit. Hence, the *K-L* model should give the same results for the two cases. This implies $D = D_{th}$ for turbulent diffusion. Thus, the expression for the sum of the enthalpy and conduction fluxes (assuming that the specific heats for each fluid are constant) is significantly simplified:

$$q_h = q_d + q_c = -\bar{\rho}D\left[\sum_{i=1}^{N}\left(\tilde{h}_i\frac{\partial \tilde{F}_i}{\partial x}\right) + c_p\frac{\partial \tilde{T}}{\partial x}\right] =$$

$$-\bar{\rho}D\sum_{i=1}^{N}\left(\gamma_i\tilde{e}_i\frac{\partial \tilde{F}_i}{\partial x} + \gamma_i c_{vi}\tilde{F}_i\frac{\partial \tilde{T}}{\partial x}\right) = \tag{57}$$

$$-\bar{\rho}D\sum_{i=1}^{N}\left(\gamma_i\tilde{e}_i\frac{\partial \tilde{F}_i}{\partial x} + \gamma_i\tilde{F}_i\frac{\partial \tilde{e}_i}{\partial x}\right)$$

$$q_h = -\bar{\rho}D\frac{\partial \tilde{h}}{\partial x} \sim -\frac{\mu_t}{N_F}\frac{\partial \tilde{h}}{\partial x} \tag{58}$$

The flux q_h should replace the flux $q_e = -\frac{\mu_t}{N_e}\frac{\partial \tilde{e}}{\partial x}$ in the energy equation (17). In order to test the validity of equation (58), a simple gedanken experiment (with the turbulent diffusivity, D, set to a constant value and zero gravitational acceleration $g = 0$) is devised based on the ansatz:

If perfect gases of different molecular mass but equal temperature and pressure begin to diffuse and mix, there should be no change in temperature.

20

Thus, an initial constant temperature profile should remain as such while the two components begin to diffuse. To test the above, we use a 1D domain of 1 m size $(-0.5 < x < 0.5)$ with the interface located at $x = 0$ m and $\bar{\rho}_1 = 20$ kg/m³, $\bar{\rho}_2 = 1$ kg/m³, $\gamma_1 = \gamma_2 = 1.4$, $D = 0.01$ m²/s and $\bar{p}_0 = 10000$ Pa. Moreover, since the temperature is constant, so should the internal energy per unit volume $\bar{\rho}_1 \tilde{e}_1 = \bar{\rho}_2 \tilde{e}_2$ be for equilibrium, hence $\bar{\rho}_1 c_{v1} = \bar{\rho}_2 c_{v2}$.

Equation (55) may now be solved analytically to give:

$$\bar{\rho} = \frac{1}{2} (\bar{\rho}_1 + \bar{\rho}_2) + \frac{1}{2} (\bar{\rho}_1 - \bar{\rho}_2) \operatorname{erf}(z) \tag{59}$$

so that the volume fraction distribution is given by:

$$f_1 = \frac{1}{2} [1 - \operatorname{erf}(z)] \tag{60}$$

with

$$z = \frac{x}{\sqrt{4Dt + w_0^2}}$$

and $w_0 = 0.02\, m$ being the initial diffuseness of the interface used in order to avoid high early time diffusive velocities.

Note that no turbulence model is used for this test, thus the inviscid (Euler) part of the equations is only retained along with the diffusional terms where the turbulent viscosity μ_{t} is replaced by $\bar{\rho}D$. We have also conducted simulations using different heat capacity ratios for the two fluids with $\gamma_1 = 2$ and $\gamma_2 = 1.4$. This requires that the following condition is additionally satisfied:

$$c_{v1} \bar{\rho}_1 (\gamma_1 - 1) = c_{v2} \bar{\rho}_2 (\gamma_2 - 1) \tag{61}$$

The simulation is performed until $t = 0.5\, s$ and the profiles of the density and normalized temperature $(10\,\tilde{T}/\tilde{T}_0)$, scaled by the initial interface temperature $\tilde{T}_0$, are plotted in Figures 2 and 3 for fluids with the same and different heat capacities, respectively. The results clearly show that the addition of the inter-diffusional enthalpy flux corrects the temperature profile, i.e., it remains constant.

All simulations conducted henceforth have used the turbulent diffusion of enthalpy, instead of internal energy (unless otherwise stated). The total energy equation (17) then recasts as follows:
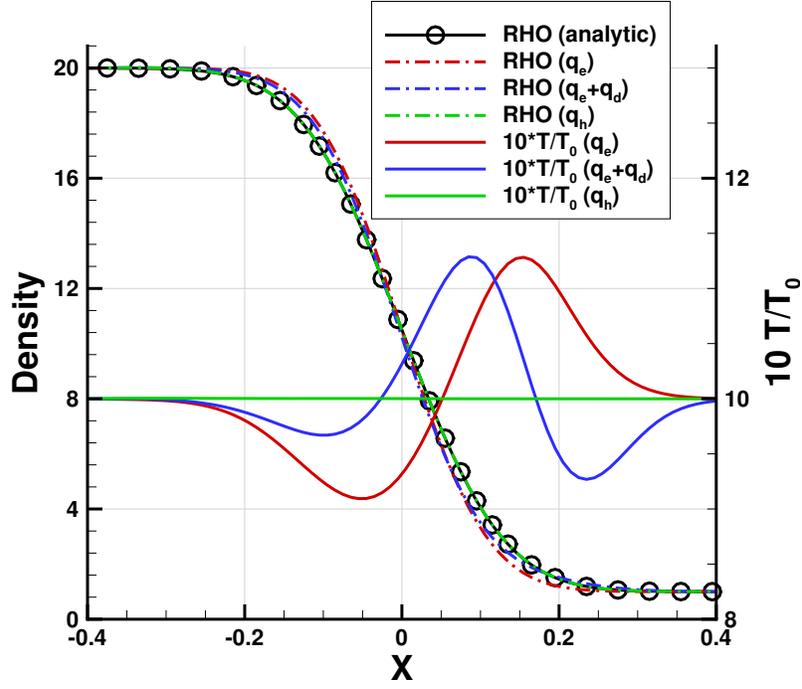
FIG. 2: Temperature and density profiles for $\gamma_1 = \gamma_2 = 5/3$.
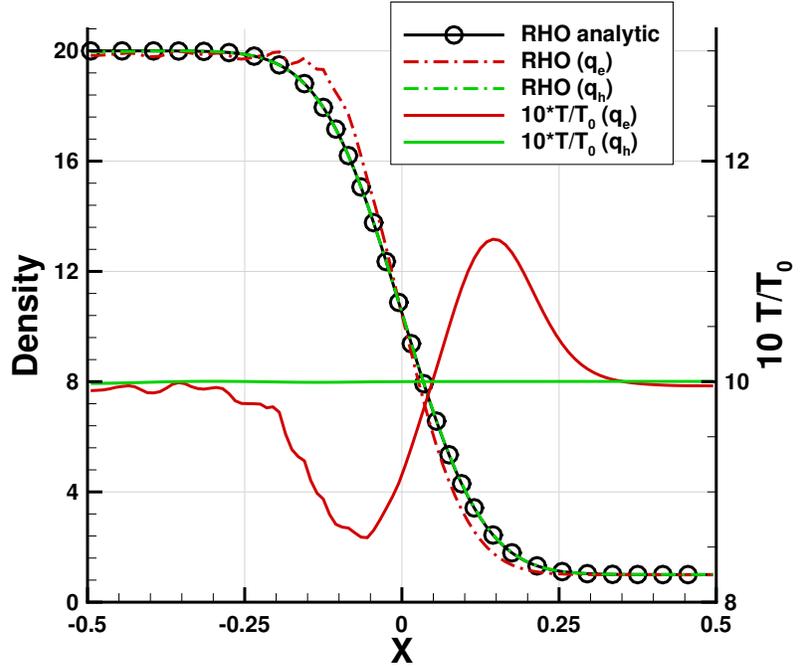
FIG. 3: Temperature and density profiles for $\gamma_1 = 2$ and $\gamma_2 = 5/3$.

22

$$\frac{\partial}{\partial t}(\bar{\rho}E^*) + \frac{\partial}{\partial x_i}(\bar{\rho}E^*\tilde{u}_i) = -\frac{\partial}{\partial x_i}(\bar{p}\tilde{u}_i) - \frac{\partial \tau_{ij}\tilde{u}_j}{\partial x_i}$$
$$+ \frac{\partial}{\partial x_i}\left(\frac{\mu_t}{N_h}\frac{\partial \tilde{h}}{\partial x_i}\right) + \frac{\partial}{\partial x_i}\left(\frac{\mu_t}{N_K}\frac{\partial K}{\partial x_i}\right) \tag{62}$$

To account correctly for the compositional change in the mass-fraction due to turbulent diffusion, the turbulence model constants for the diffusion of mass fraction, N_F, and enthalpy, N_h, must be equal ($N_F = N_h$). The flux of the turbulent diffusion of mass per unit volume of each species $(\mu_\tau/N_F)\,\partial F_i/\partial x$ carries with it a corresponding amount of specific enthalpy h_i, which comprises the sum of the specific internal energy (e_i) and the product of the pressure and specific volume (p/ρ_i), all functions of the state of the thermodynamic system. Thus, there exists an inter-diffusion enthalpy flux term [48] associated with the diffused mass-flux, which under the current K-L model assumptions is defined as $h_i\,(\mu_\tau/N_F)\,\partial F_i/\partial x$. If the diffusion coefficients N_F and N_h were to be different, then the diffusion of enthalpy would not satisfy the above physical process. This is also obvious noticing that the laminar viscosity ρD is replaced by the turbulent μ_τ/N_F in (58).

It is worth mentioning that Morán-López and Schilling [24, 25] also included an inter-diffusional enthalpy flux term in their K-ε model. However, a different formulation was used. In [24, 25], three terms, heat conduction, internal energy diffusion and inter-diffusional enthalpy flux, were used to model the flow of internal energy, whereas in this paper a single term, the diffusion of total enthalpy is used.

Further results on the influence of the inter-diffusional enthalpy flux in RTI mixing are presented in section III E.

III. RAYLEIGH-TAYLOR MIXING

The turbulence models have been applied to 1D RT cases with density ratios 3:1 and 20:1 (ρ_1=3g/cm^3 or 20g/cm^3 and ρ_2=1g/cm^3). The computational domain has dimensions [-8, 20] cm with the heavy fluid placed on the left side of the domain and the initial interface at x=0. Unless otherwise stated, the computational grid consists of 100 cells and the adiabatic exponent is γ=5/3 for both fluids. The following relation is satisfied in all cases $A_0 g$=1, thus for density ratio 3:1 the gravitational acceleration is g=2cm/s^2 and for 20:1 is $g \approx$1.105cm/s^2.

Note that from the measuring units given to the physical properties of the fluids, it naturally follows that time is measured in seconds.

Comparisons between the models are presented for the normalized turbulent kinetic energy (K/K_{max}) and volume fraction (VF) profiles vs. X/W as well as for the evolution of the mixing width W and maximum turbulent kinetic energy K_{max}. The mixing width is defined by $W = \int f_1(1 - f_1)dx$, where f_1 is the dense fluid volume fraction. For the two fluid model, the single-fluid TKE (K_1) is defined by $K_1 = K + 1/2\ F_1F_2(u_1 - u_2)^2$, where K is the TKE in the two-fluid model, and $F_{1,2}$, $u_{1,2}$ are the fluid mass fractions and velocities, respectively.

With regard to the initial conditions, the two fluids are considered to be in isentropic hydrostatic equilibrium, i.e. $\tilde{u}=0$ and $\bar{p}/\bar{\rho}^{\gamma} = $ constant within each fluid, where γ is the ratio of specific heats $(\gamma = c_p/c_v)$. The initial pressure and density profiles are obtained by integrating $dp/dx = \rho g$, hence

$$
\bar{p}_0(x) =
\begin{cases}
\bar{p}_{0\mathrm{I}}\left[1 + \dfrac{\gamma - 1}{\gamma}\dfrac{\bar{\rho}_{0\mathrm{H}}}{\bar{p}_{0\mathrm{I}}}g(x - x_\mathrm{I})\right]^{\frac{\gamma}{\gamma-1}} & x < x_\mathrm{I} \\[2em]
\bar{p}_{0\mathrm{I}}\left[1 + \dfrac{\gamma - 1}{\gamma}\dfrac{\bar{\rho}_{0\mathrm{L}}}{\bar{p}_{0\mathrm{I}}}g(x - x_\mathrm{I})\right]^{\frac{\gamma}{\gamma-1}} & x \geq x_\mathrm{I}
\end{cases}
\tag{63}
$$

$$
\bar{\rho}_0(x) =
\begin{cases}
\bar{\rho}_{0\mathrm{H}}\left[1 + \dfrac{\gamma - 1}{\gamma}\dfrac{\bar{\rho}_{0\mathrm{H}}}{\bar{p}_{0\mathrm{I}}}g(x - x_\mathrm{I})\right]^{\frac{1}{\gamma-1}} & x < x_\mathrm{I} \\[2em]
\bar{\rho}_{0\mathrm{L}}\left[1 + \dfrac{\gamma - 1}{\gamma}\dfrac{\bar{\rho}_{0\mathrm{L}}}{\bar{p}_{0\mathrm{I}}}g(x - x_\mathrm{I})\right]^{\frac{1}{\gamma-1}} & x \geq x_\mathrm{I}
\end{cases}
\tag{64}
$$

where $\bar{p}_{0\mathrm{I}}$ is the initial pressure at the interface; $\bar{\rho}_{0\mathrm{H}}$ and $\bar{\rho}_{0\mathrm{L}}$ are the initial densities of the heavy (left side) and light (right side) fluids, respectively; x_I is the position of the interface. The two-fluid and K-L models are initialized in a similar way. The calculation begins when the mixing zone is 2-3 meshes wide, according to the self-similar growth law (1). The above conditions are used outside the initial mixing zone together with $K=L=0$ and $U_1=U_2=0$ (the velocities of the two fluids). For the K-L model, within the mixing zone, a simple approximation is used for $K_0 = |A_0|g\eta_0$, while L_0 and η_0 are related to the mixing width of the fine grid ILES: $L_0 = \eta_0{}^2/\Delta x$, where A_0 is the initial Atwood number and $\eta_0 = \Delta x/4$ is the initial amplitude of the perturbation. Note that L_0 and η_0 are not dependent on the

grid resolution used in the K-L model simulations. The value of Δx is simply related to the fine grid ILES that (based on non-dimensional units) used perturbation standard deviation $\sim 0.0005 L_{max}$ with $L_{max} = 500$, i.e., $\sim \Delta x/4$, where Δx is the cell width.

The TF calculation is initialized by integrating the buoyancy-drag model [17], which consists of an ordinary differential for the bubble and spike distances and velocities, h_1, h_2, $\dot{h}_1$, $\dot{h}_2$, up to the time $t = 2$. For the simple test case, this is equivalent to obtaining h_1, $\dot{h}_1$ from equation 1 and h_2, $\dot{h}_2$ from a similar equation for the spike distance (the depth to which the mixing zone extends into the lighter fluid 2). Fluid volume fractions, $\hat{f}_s$, are then set within the mixing zone $(-h_1, +h_2)$ to give a profile which approximates the self-similar distribution. The initial length scale within the mixing zone is set to $L = h_1$ and the turbulence kinetic energy is set to $K = 4K_{max}\hat{f}_1\hat{f}_2$ with $K_{max} \propto \dot{h}_1^2$. Finally mass is exchanged between the two initial fluids in the mixing zone in order to initialize the phase variables, f_r, α_{rs}. The extent of the mass exchange is chosen to give the required value of the molecular mixing parameter (equation 65). The initialization is chosen to trigger self-similar mixing without significant over-shoots or under-shoots and makes a key contribution to reducing the effect of mesh size.

The RTI mixing results are split into two parts, one containing an investigation of a heavy-to-light density ratio of 3:1 (initial Atwood number $A_0 = 0.5$), and the other 20:1 ($A_0 \approx 0.905$). For each Atwood number, a series of tests are conducted to examine the single and two-fluid models sensitivities and dependencies on various physical conditions. The dependence of the solution on the initial interface pressure is investigated and a grid convergence study is performed to examine the effects of grid resolution. Furthermore, the effects of different heat capacity ratios (γ) for the two fluids on the turbulence modeling results is also investigated. For the assessment of the turbulence models, we examine the spatial profiles of the volume-fraction (VF) and normalized turbulent kinetic energy (K/K_{max}) vs. X/W as well as the self-similar growth of the integral mixing width (W) and maximum turbulent kinetic energy (K_{max}) vs. self-similar time (A_0gt^2).

Note that for self-similar turbulent mixing at a given density ratio, both W and K_{max} grow at a constant rate equivalent to A_0gt^2. Since for the cases considered here $A_0g = 1$, both W and K_{max} are plotted against t^2. The late-time gradients of the curves are noted in tables III and V.

A. Comments on Large Eddy Simulations

A complete description of the implicit large eddy simulations (ILES) used in this study can be found in [9]. The ILES results have been obtained by using the TURMOIL Lagrange-remap hydro-code which calculates the mixing of compressible fluids. The TURMOIL hydro-code solves the Euler equations plus advection equations for fluid mass fractions. The Lagrange-remap method was first used for RT mixing by Youngs [39]. More details of the method, its application to RT and Richtmyer-Meshkov mixing and further discussion of MILES and other ILES techniques are given in Grinstein et al. [8]. Direct numerical simulation (DNS) is feasible at moderate Reynolds number and is essential for assessing the influence of Reynolds number and Schmidt number. It is argued here that high-resolution ILES is the most computationally efficient way for calculating the high-Reynolds number behavior and that this approximation was needed to make the series of simulations presented by Youngs [9] feasible. As in previous ILES studies for RT mixing, the present ILES [9] were conducted under the assumption that the Reynolds number is high enough to have little effect on the main quantities required for engineering application. In particular, the Reynolds number is assumed to be high enough for the effect of the Schmidt number to be unimportant, i.e., the flow is beyond the mixing transition as defined by Dimotakis [51]. For RT mixing a suitable definition of the Reynolds number is $Re = h_1 \dot{h}_1 / \nu$, where h_1 is the extent of the mixing zone and ν is the kinematic viscosity. According to the experimental results (see [51, 52] and references therein) the mixing transition corresponds to Re $\sim 10^4$. The results shown in this paper are applicable to high Reynolds number mixing in which Re exceeds 10^4 .

Previous results for variable density RT flows at Atwood numbers up to 0.5 [53–55] have shown that mixing becomes qualitatively different at high density ratios compared to when the densities are commensurate in the Boussinesq approximation limit. Specifically it is found that the location of peak turbulence kinetic energy, K, moves into the light fluid side as the Atwood number increases. Subsequently, the molecular mixing proceeds differently either side of the RT layer. Another consequence observed in [6] when simulating a 0.5 Atwood number RT flow, is that the penetration distance of the pure heavy fluid is larger than that of the pure light fluid [53, 54]. This mixing asymmetry (higher growth rate in the spike regions compared to the bubble regions), also observed experimentally, increases as
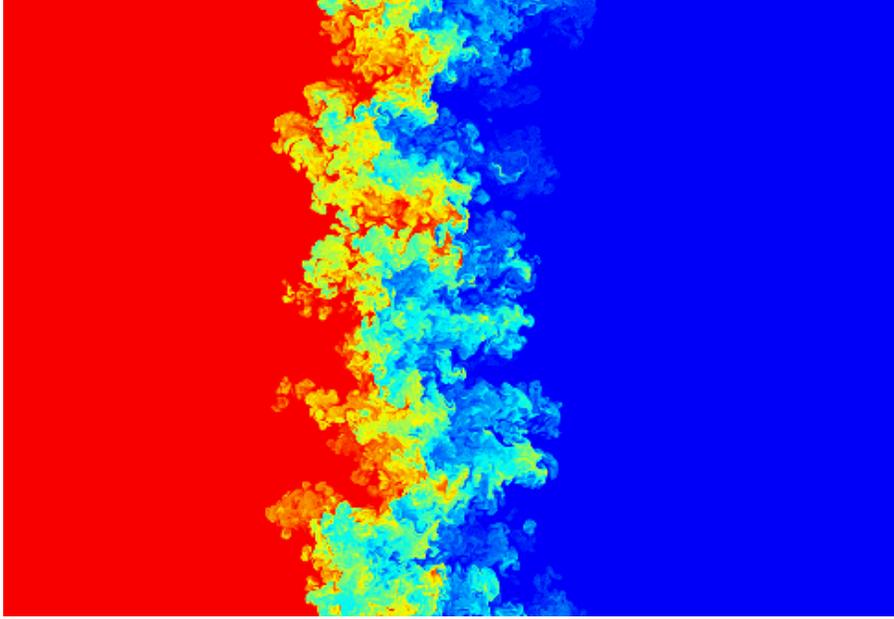
FIG. 4: ILES contours of volume fraction for density ratio 3:1

the Atwood number increases. Such physical processes need to be captured and modelled correctly by a mixing model in order for it to be deemed successful and for it to be applicable over a wide range of cases. As such, the mixing models examined herein are tested under two different density contrasts, a low 3:1 and high 20:1 heavy to light fluid density ratios. The volume fraction contours from the ILES are shown in Figs 4 and 5 for density ratios 3:1 and 20:1 respectively. The ILES results from [9] which are used here, are obtained from very high resolution simulations, typically using $2000 \times 1000 \times 1000$ size meshes, and it is argued that the results used are mesh-converged to the point that the effect of the unresolved scales is negligible. For some of the cases considered in [9], DNS results are available [50] that are very similar to the ILES results.

B. Summary of K-L turbulence model modifications

The key modifications in the original K-L model [22] are:

1. The turbulent internal energy diffusion term is replaced by the turbulent diffusion of enthalpy;

2. The local Atwood number and cell-center gradients are calculated using equations (44)-(47);

27
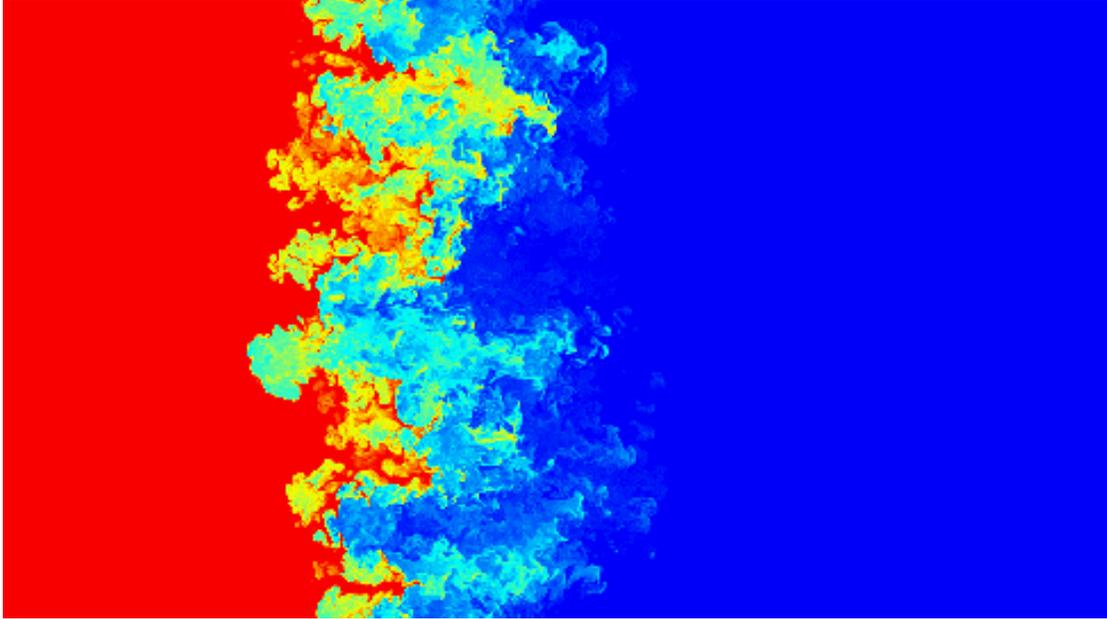
FIG. 5: ILES contours of volume fraction for density ratio 20:1

To assess the effects of these modifications, we employ the RT case with a density ratio of 20:1 and an initial interface pressure of p_0=1000 dyn/cm^2. Figure 6 shows the results obtained for the volume fraction (VF) and normalized turbulent kinetic energy (K/K_{max}) using the original K-L model (depicted by sup-script o) and with the aforementioned modifications (depicted by sup-scipt m). Evidently, the proposed modifications lead to better agreement with ILES [9] for both quantities examined. Therefore, the results presented in the rest of the paper have been obtained using the modified K-L model.

C. Density Ratio 3:1

The self-similar growth rate parameters of W and K_{max} are important to capture correctly during model calibration. Theory in the self-similar regime of the RT instability indicate that the bubble distance h_b, defined as the most extreme location where the light fluid has penetrated the heavy and is of at least 1% volume fraction, is given by $h_b = \alpha A g t^2$.

As already mentioned in Section II A 2, a self-similar growth rate parameter of $\alpha = 0.06$ giving $h_b = 0.06 A g t^2$ is presently used as indicated by ILES [9]. In addition, the high-resolution ILES [9] found that the mixing width W scales with the bubble height h_b as $h_b = \beta W$, where $\beta = 3.433 - 0.387 A^2$. This then allows for the calculation of the growth
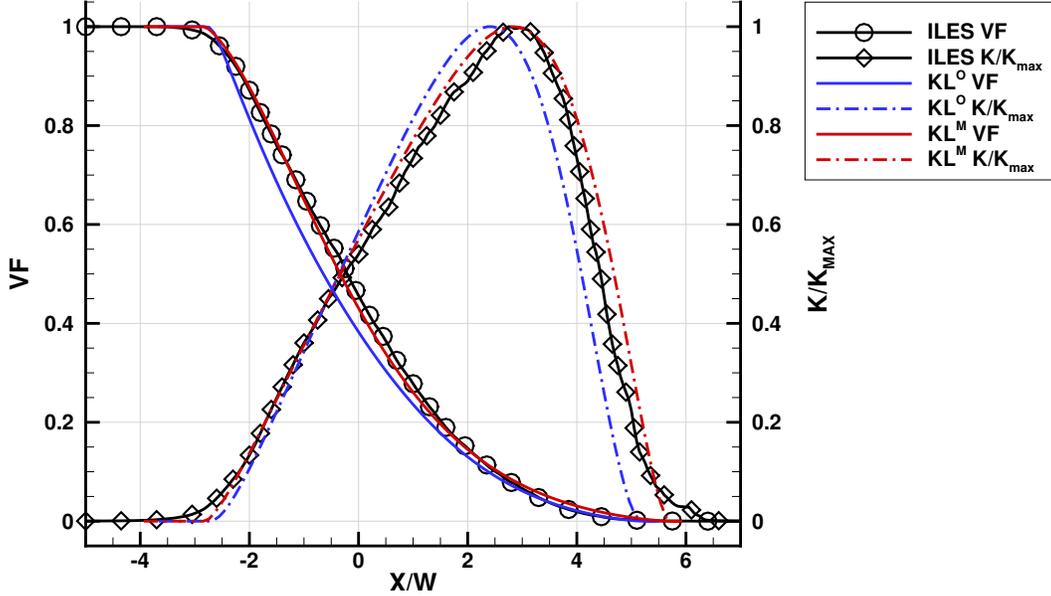
FIG. 6: VF and K/K_{max} profiles comparison of the two different K-L model approaches against ILES.

Case	W	K_{max}
ILES	0.017984	0.010
TF	0.018247	0.009958
K-L	0.018077	0.009536

TABLE III: Self-similar growth rate parameters of W and K_{max}

for density ratio 3:1; $p_0 = 500 \mathrm{dyn/cm}^3$ and $\gamma_1 = \gamma_2 = 5/3$

rate parameter of W. Comparison of the TF and K-L models results with ILES for the late time growth rate parameters of W and K_{max} are presented in Table III.

1. Effect of initial interface pressure

Calculations using both models have been performed for different initial pressures at the interface (p_0=250, 500, 2000 dyn/cm^2) in order to assess the incompressibility limit of the models. The results are included in Figures 7-8. The growth of W is similarly predicted by both models. In the case of the K-L model, there is only a slight effect of the initial interface pressure on W (Figure 7), whereas the TF results remain largely unchanged. The reason for

29

(a) W (b) K_{max}
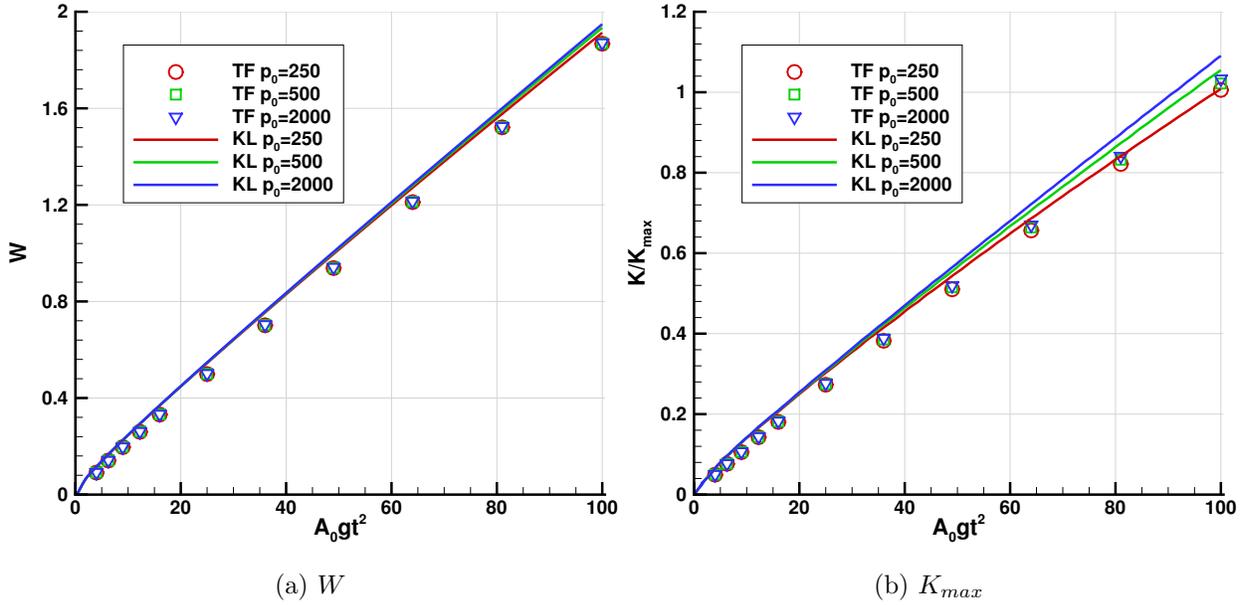
FIG. 7: Time evolution of mixing width and maximum turbulent kinetic energy for RTI mixing of fluids with initial density ratio 3:1. Different initial interface pressures.

the larger value of W with increasing initial interface pressure is also linked to the higher K_{max}, thus resulting in a larger turbulent viscosity μ_t and mass-fraction diffusion. Though the final value ($t = 10$, $A_0 g t^2 = 100$) for K_{max} also increases with higher initial interface pressure in the TF model, it is more pronounced in the case of the *K-L* model.

Figures 8a and 8b show the VF and K/K_{max} profiles, respectively, at two time instants for the RT case with density ratio 3:1 and initial interface pressure $p = 500$ dyn/cm^2. Comparisons are also presented with ILES [9]. The (3D) ILES results ($t = 10$ sec.) have been spatially averaged to allow comparisons with the 1D turbulence model calculations. The K_{max} and W profiles show that both turbulence models achieve self similar solutions. The VF profiles are almost identical and in excellent agreement with ILES. Some minor discrepancies appear in the K/K_{max} profiles, especially on the spike side, where the TF and *K-L* results agree closely.

2. Grid Convergence study

In this section, the effects of grid resolution on the results is investigated by doubling the number of cells twice, starting from the original discretization of 100 cells. Hence the grid

(a) VF vs X/W

(b) K/K_{max} vs X/W
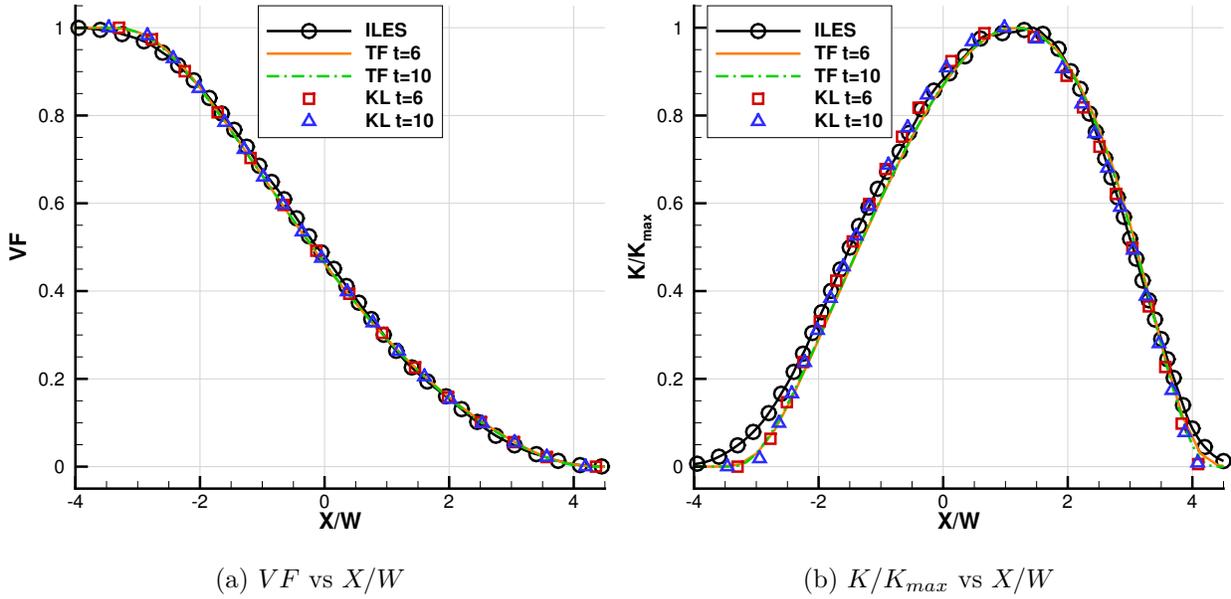
FIG. 8: Volume fraction (a) and Turbulent kinetic energy (b) profiles for RTI mixing of fluids with initial density ratio 3:1.

convergence study has been carried out using three grids with $N_x = 100$, 200 and 400 cells, respectively.

The reduction in numerical dissipation associated with the cell size (filter) is apparent only at the early stages of the simulation, until the turbulent viscosity of the model becomes large enough to have a greater effect on the results than the numerical dissipation of the convection terms. This is shown in the integral mixing width (W) and maximum turbulent kinetic energy (K_{max}) results in Figures 9-10. The grid resolution seems to have an effect on the growth rate only at the early stage of the simulation. Once the turbulence viscosity becomes sufficiently large, all grids achieve a similar growth rate. This is further supported by the negligible differences in the profiles of K/K_{max} and W, for both the $K - L$ and TF models, shown in Figures 10a and 10b.

For the $K - L$ model the reduction in numerical dissipation due to the increasing grid resolution occurs primarily at the beginning of the simulations, during which there is a noticeable gradual divergence of the mixing width (W) and maximum turbulent kinetic energy (K_{max}) growth rates up until the turbulence model diffusion becomes the leading cause. Due to this difference in initial growth rate, the results provided by the finer grids appear to be "delayed" in comparison to the coarser grids. For the TF model, the integral
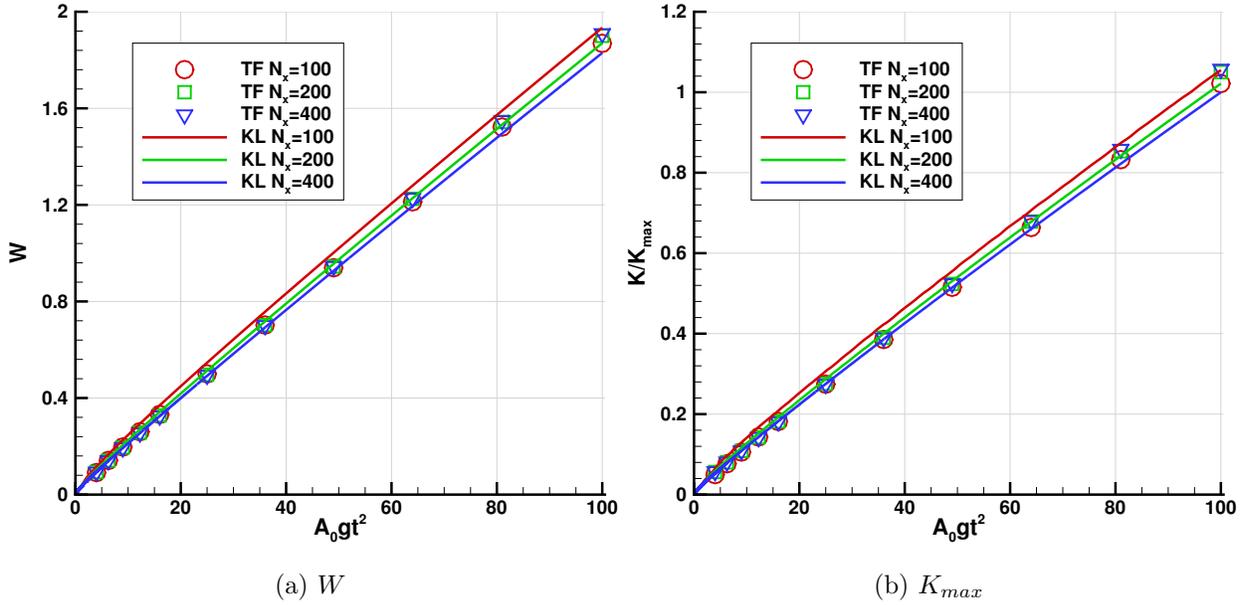
FIG. 9: Time evolution of mixing width and maximum turbulent kinetic energy for RTI mixing of fluids with initial density ratio 3:1. Effect of grid resolution.

mixing width shows little variation with mesh. As already noted, the initial conditions model is used to minimize this variation. For K/K_{max} there are also small "delays" due to the change in mesh size. For both the $K-L$ and TF models the effect of mesh size for this simple test is small and not significant for practical applications.

D. Density Ratio 20:1

Several calculations were performed for different interface pressures and specific heat capacities. A summary of the test cases are presented in Table IV.

In addition to investigating the TF and K-L models behavior for different interfacial pressures and specific heat capacity ratios, we have performed a series of tests for the K-L models to examine the effects of: i) turbulent diffusion of internal energy term (section III E), i.e., comparing the results obtained using equation (17) (internal energy diffusion) to those of equation (62) (enthalpy diffusion); and ii) calculation of the local Atwood number (Section III F), using equations (37)-(43) or (44)-(47).

Comparison of the results for the late time growth rate parameters of W and K_{max} between the TF and K-L models and ILES, are presented in Table V for the case of 20:1.
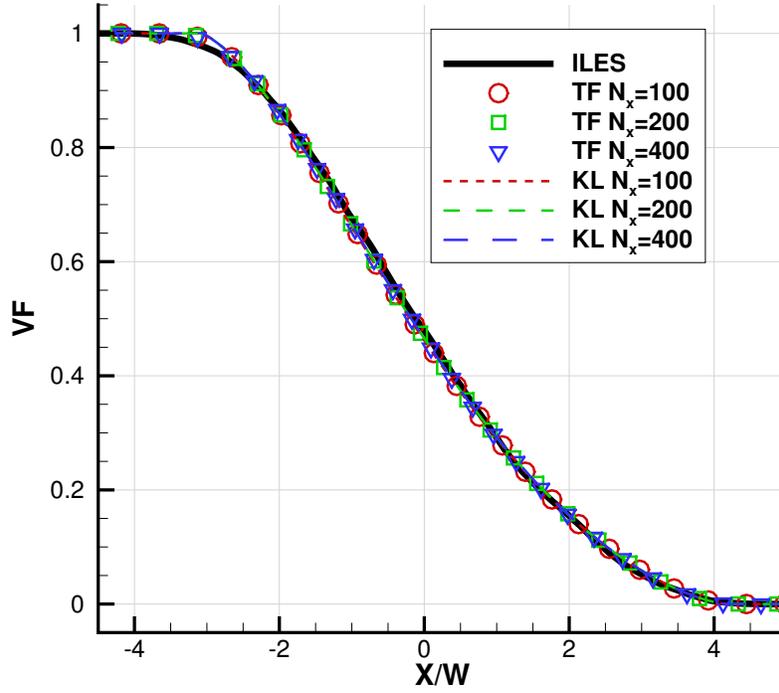
(a) VF vs X/W
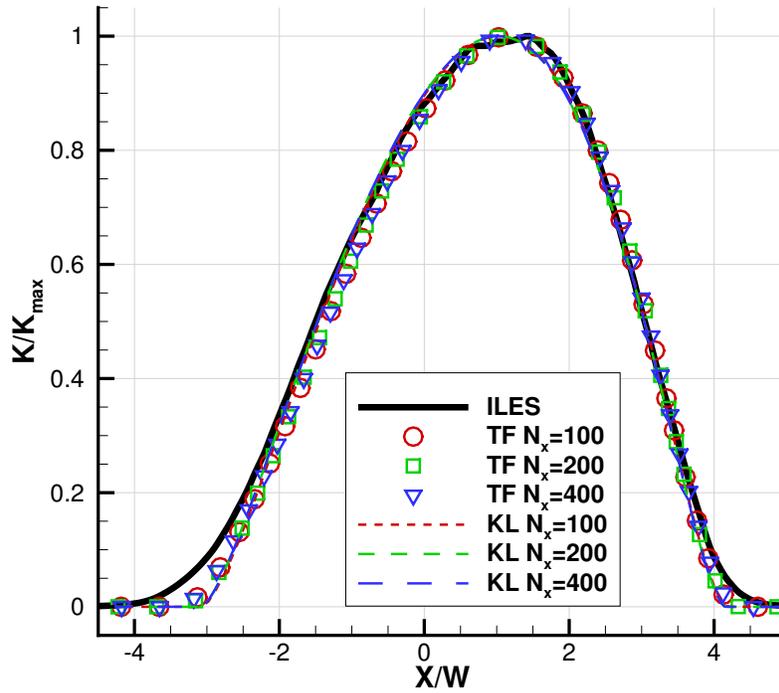
(b) K/K_{max} vs X/W

FIG. 10: Volume fraction (a) and Turbulent kinetic energy (b) profiles for RTI mixing of fluids with initial density ratio 3:1. Effect of grid resolution.

Case	p_0 (dyn/cm^2)	γ_1	γ_2
1	1000	5/3	5/3
2	2000	5/3	5/3
3	4000	5/3	5/3
4	1000	2	2
5	1000	4	5/3

TABLE IV: Simulations carried out for density ratio 20:1

Case	W	K_{max}
ILES	0.019254	0.0170
TF	0.019410	0.015407
K-L	0.018964	0.015157

TABLE V: Self-similar growth rate parameters of W and K_{max}

for density ratio 20:1; $p_0 = 2000$ dyn/cm^3 and $\gamma_1 = \gamma_2 =$5/3

Both turbulence models are in fairly good agreement with ILES, however the TF model provides overall better results.

1. *Effect of initial interface pressure*

Calculations have been performed for fluids of an initial density ratio 20:1 and equal specific heat capacity ratios $\gamma_1 = \gamma_2 = 5/3$. The parameter altered is the initial interface pressure, ranging p_0=1000, 2000 and 4000 dyn/cm^2, in order to assess the incompressibility limit of the turbulence models. Self-similarity is achieved (Figure 11) by both models while the change in the initial interface pressure has almost negligible effect in either model.

The VF and K/K_{max} results at different time instants and for initial interface pressure of $p = 4000$ dyn/cm^2 (Case 3) are shown in Figures 12a and 12b, respectively. Similar to the 3:1 density ratio, the VF results are nearly identical and in very good agreement with ILES. Furthermore, the TF and K-L results for K/K_{max} are in very good agreement with ILES. While the two models accurately predict the peak location and edges, there are some

(a) W (b) K_{max}
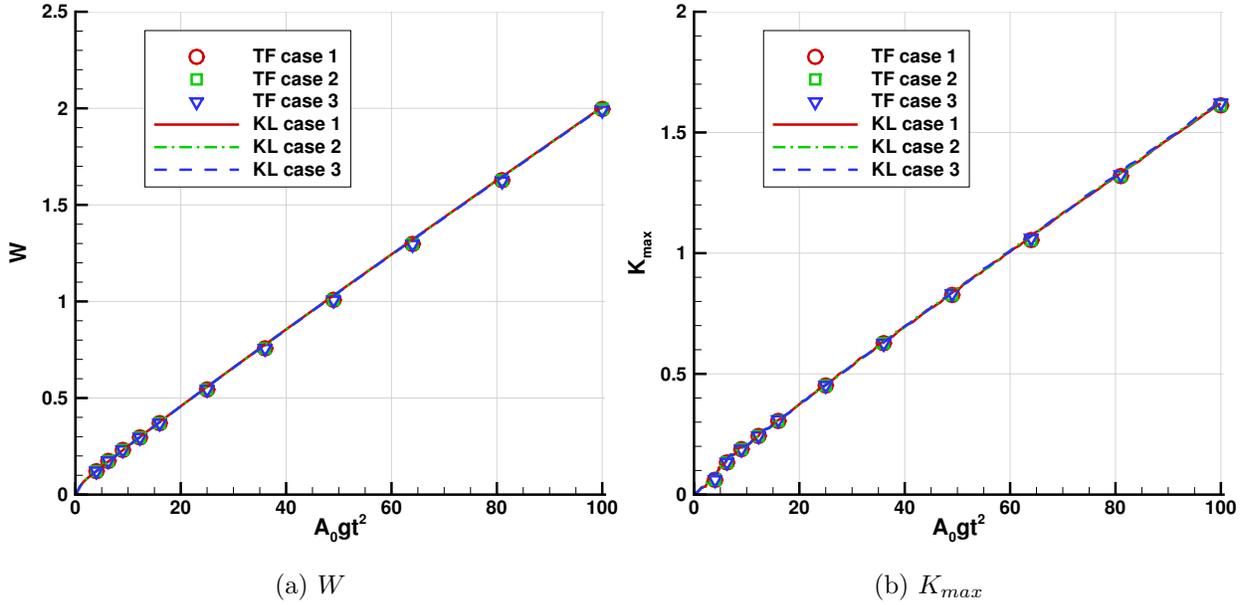
FIG. 11: Time evolution of mixing width and maximum turbulent kinetic energy for RTI mixing of fluids with initial density ratio 20:1. Different initial interface pressure p_0.

discrepancies in the results in the "sloped" regions. In some areas the TF model seems to be more accurate, such as the slope around the peak of K/K_{max}, while the K-L model appears to be more accurate around the edges of the instability.

2. Effect of heat capacity ratio

To further assess the behavior of the models, calculations were performed by altering the values of specific heat ratio for both fluids: $\gamma_1 = \gamma_2 = 2$, as well as $\gamma_1 = 4$, $\gamma_2 = 5/3$ (Cases 4 and 5 in Table IV). Figure 13 shows that W and K_{max} correctly retain their self-similar growth rate and magnitude for all specific heat ratio combinations tested. This is indicative of the correct thermodynamic closure of both the TF and K-L model and, as it will be shown in the next section, in the case of the K-L model it is a direct result of using the turbulent diffusion of enthalpy.

E.   Effect of Enthalpy Diffusion

In section II D, a gedanken test-case was used to justify the substitution of the turbulent diffusion of internal energy per unit mass by the specific enthalpy as proposed by Cook [48].

(a) VF vs X/W (b) K/K_{max} vs X/W
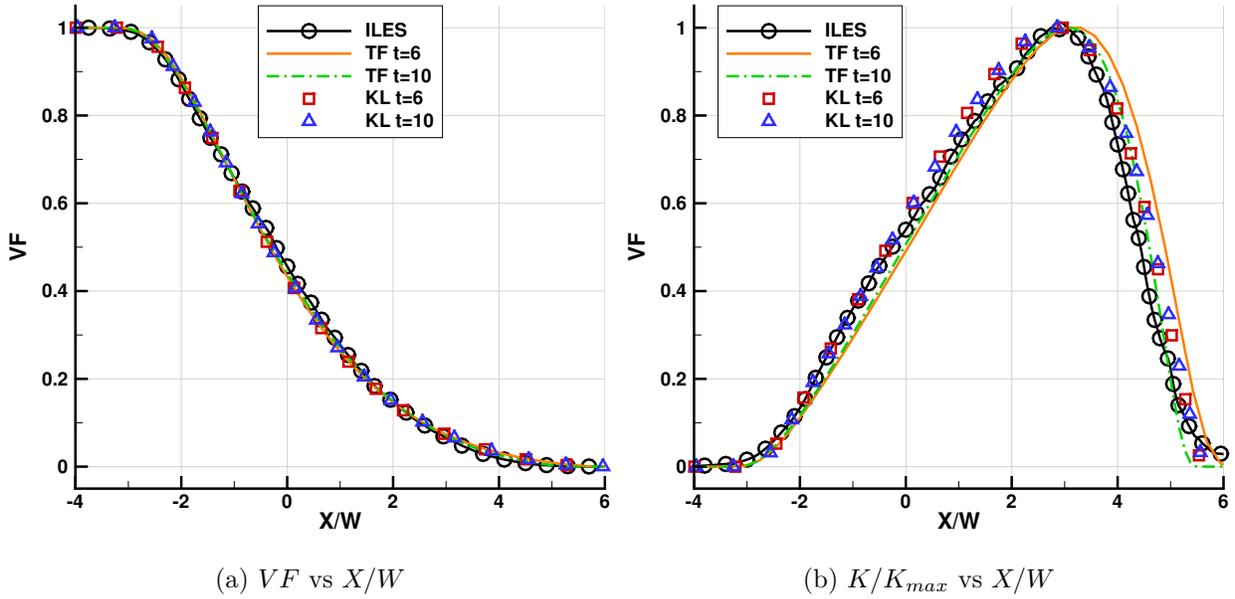
FIG. 12: Volume fraction (a) and normalized turbulent kinetic energy (b) profiles for RTI mixing of fluids with initial density ratio 20:1.

It was shown that the conservation form of the total energy equation ($\bar{\rho}E^*$) using equation (17) should be reformulated as equation (62). The effects of the above terms will also be discussed in this section for the 20:1 RT case with $\gamma_1 = 4$ and $\gamma_2 = 5/3$ (Case 5 in Table IV).

The effects of the enthalpy term are significant for the maximum turbulent kinetic energy K_{max} and nearly negligible on the mixing width W (Figure 15). The implementation of turbulent enthalpy diffusion gives growth rates for W and K_{max} similar to the TF model. Furthermore, the VF (Figure 14a) and K/K_{max} (Figure 14b) profiles are significantly improved, matching closely those obtained by the TF model and ILES.

The effects of the enthalpy vs. internal energy diffusion on the temperature profile are shown in Figure 16. The temperature profile at t=10 sec has been normalized by the initial interface temperature corresponding to $p_0 = 1000$ dyn/cm^2, while satisfying the condition (61). The results correspond to Cases 1 and 5 of Table IV. Introduction of the enthalpy flux q_h instead of q_e in the K-L model, leads to similar results to the TF model. In contrast, when using the diffusion of internal energy (17) in the K-L model, an unphysical wave-like oscillation in temperature occurs.

(a) W　　　　　　　　　　　　　(b) K_{max}
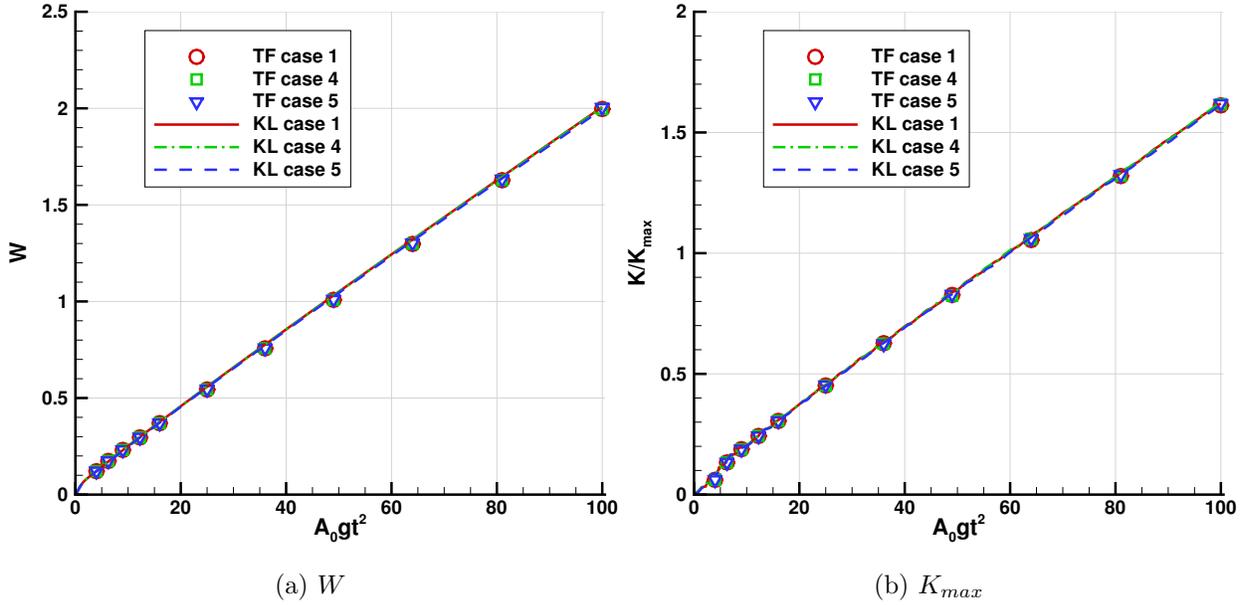
FIG. 13: Time evolution of mixing width and maximum turbulent kinetic energy for RTI mixing of fluids with initial density ratio 20:1. Different specific heat ratios γ.

F.   Effect of local Atwood number estimation

In this section, the original formulation for calculating the local Atwood number based on equation (37) is compared to that of equation (47), which makes use of the density values obtained during the reconstruction process (see section II B). Case 2 was selected in order to reduce the effect of any other parameter influencing the end results. The local Atwood numbers A_{Li} and $A_{Li/dx}$ will refer to the results obtained using equations (37) and (47), respectively.

A significant difference can be observed in Figure 17 for the self-similar growth rate of K_{max}, which initially is too large when using A_{Li}. In contrast, $A_{Li/dx}$, closely matches the TF results throughout the simulation. Consequently, the growth rate of the integral mixing width (W) is overestimated. At late times the self similar growth rates of both W and K_{max} become similar since both for A_{Li} and $A_{Li/dx}$, as $L/\Delta X$ tends to infinity $(^{L}/_{\Delta x} \to \infty)$ the initial Atwood number approaches zero $(A_{0i} \to 0)$ due to the reduced density gradient of the heavily diffused mixing width.

The effects of A_{Li} and $A_{Li/dx}$ on VF are negligible. On the other hand, the effects are significant for the normalized turbulent kinetic energy K/K_{max}. The spike and bubble locations of the RT instability are less accurately captured using the A_{Li} approach, e.g., the

(a) VF vs X/W (b) K/K_{max} vs X/W
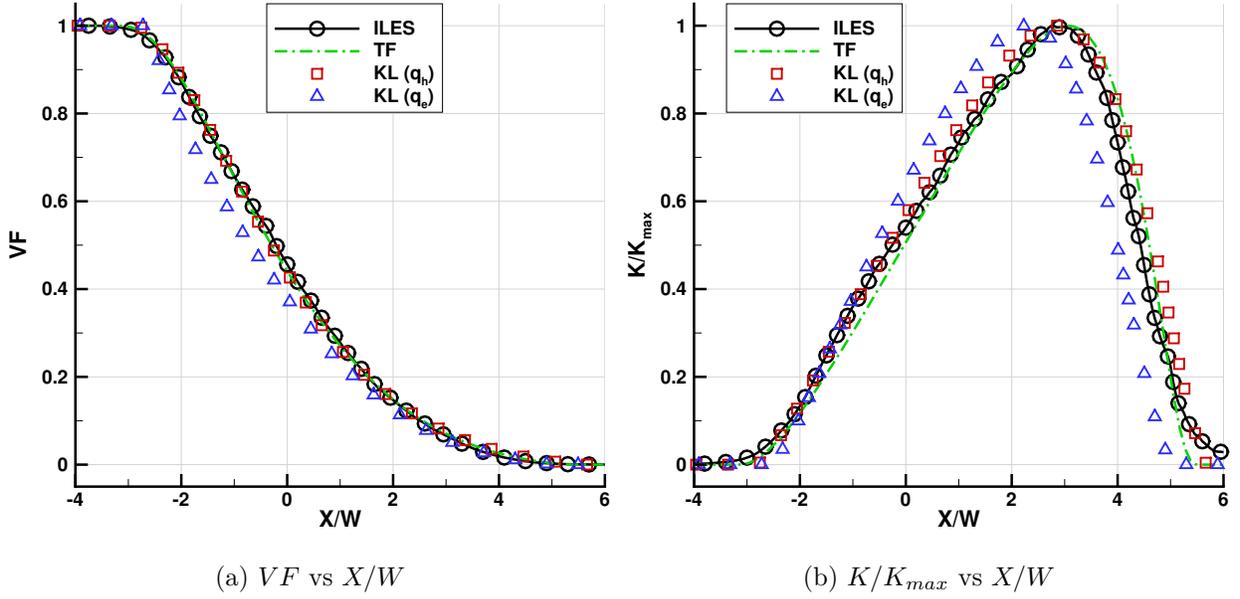
FIG. 14: Volume fraction (a) and normalized turbulent kinetic energy (b) profiles for RTI mixing of fluids with initial density ratio 20:1. Effect of enthalpy diffusion term.

K/K_{max} profile around the spike (right section of profile) is not in agreement with neither the TF model, ILES nor the K-L model using $A_{Li/dx}$.

G. Molecular Mixing in the Two-Fluid Model

A key advantage of the TF model is its ability of representing the degree of molecular mixing in a direct way, by transferring mass between the two phases. At a given value of x the mixture is represented by two components (phases), one rich in initial fluid 1 and one rich in initial fluid 2. For mixing of incompressible fluids the degree of molecular mixing at a given value of x may be conveniently expressed in terms of fluid volume fractions. For 3D distributions, a molecular mixing parameter may be defined as [9, 19, 50]:

$$\theta(x) = \frac{\langle f_1 f_2 \rangle}{\langle f_1 \rangle \langle f_2 \rangle} \qquad (65)$$

where $\langle \phi \rangle$ denotes either the plane average or ensemble average of ϕ.

The degree of molecular mixing for the layer as a whole may be quantified by a global molecular mixing parameter:

$$\Theta = \frac{\int \langle f_1 f_2 \rangle dx}{\int \langle f_1 \rangle \langle f_2 \rangle dx} \qquad (66)$$

(a) W (b) K_{max}
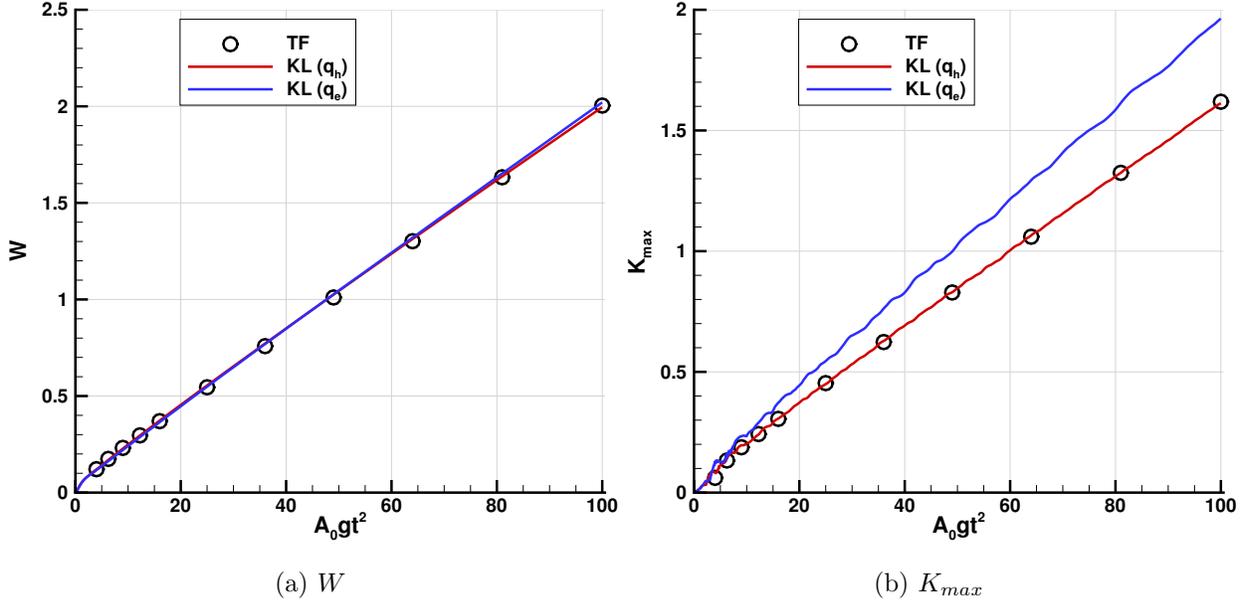
FIG. 15: Time evolution of mixing width and turbulent kinetic energy for RTI mixing of fluids with initial density ratio 20:1. Effect of enthalpy diffusion term.
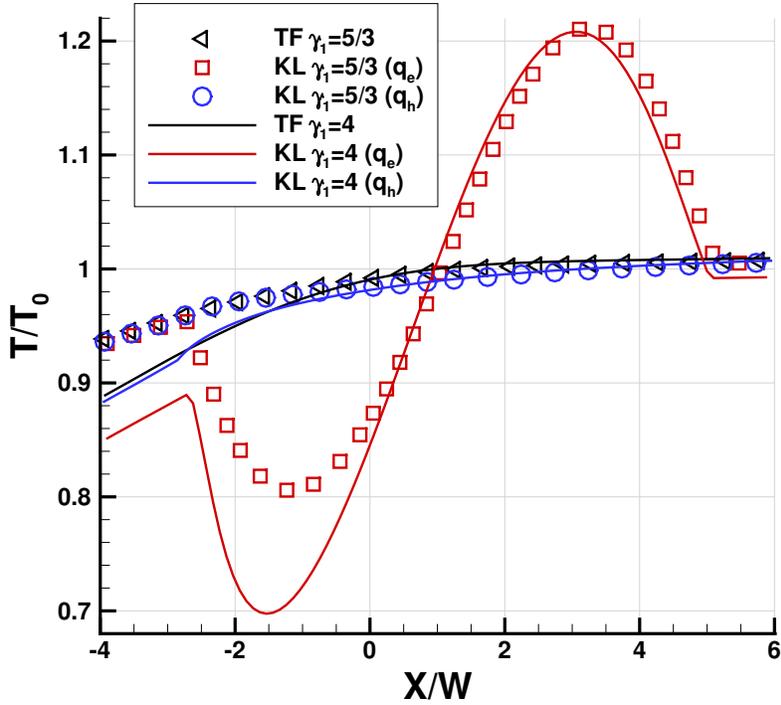
FIG. 16: Comparison of normalized temperature (T/T_0) profiles between internal energy and enthalpy diffusion terms for density ratio 20:1 cases 1 and 5 at t=10 sec.

(a) W (b) K_{max}
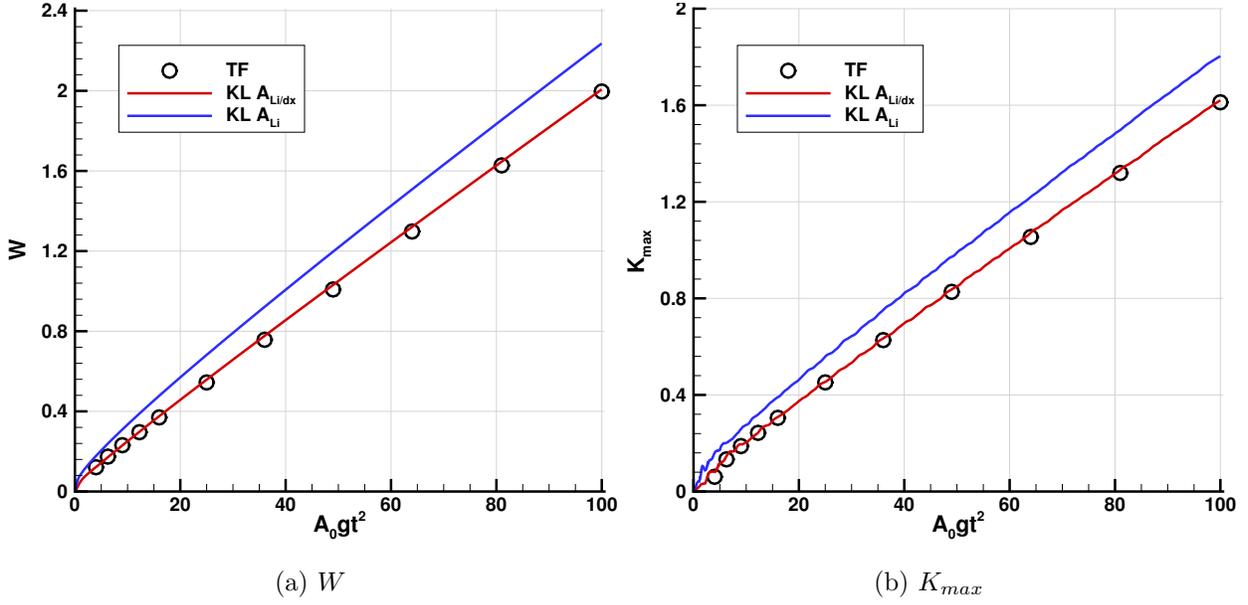
FIG. 17: Time evolution of mixing width and turbulent kinetic energy for RTI mixing of fluids with initial density ratio 20:1. Effect of local Atwood number term.

Both $\theta(x)$ and Θ lie within the range 0 (no molecular mixing) to 1 (homogeneous mixing at each x-level).

For the TF model the equivalent molecular mixing parameter is:

$$\theta(x) = \frac{f_1\alpha_{11}\alpha_{12} + f_2\alpha_{21}\alpha_{22}}{(f_1\alpha_{11} + f_2\alpha_{21})(f_1\alpha_{12} + f_2\alpha_{22})} \quad (67)$$

The global mixing parameter is calculated in a similar way. The parameter c_3 in the TF model (section II A) is chosen so that the global mixing parameter from the model matches that from the ILES simulations for the required values of A and α.

Figures 19a and 19b show plots of $\theta(x)$ at $t = 10$ for the two density ratios. The TF model results are compared with those from the ILES simulations [9]. Values of $\theta(x)$ on the low-density side are higher than those on the high-density side. This is attributed to the increased velocity fluctuations on the low-density side (see figures 8b and 12b). The effect is significantly greater at the higher density ratio. The TF model gives a very good representation of the variation of $\theta(x)$ across the mixing layer. For $\bar{\rho}_1/\bar{\rho}_2 = 20$ the values of $\theta(x)$ are slightly higher in the TF model than for ILES. This is because the available ILES data corresponds to $\alpha = 0.08$, a higher value than that used for the model calibration (reference [9] shows that Θ reduces as α increases).

(a) VF vs X/W (b) K/K_{max} vs X/W
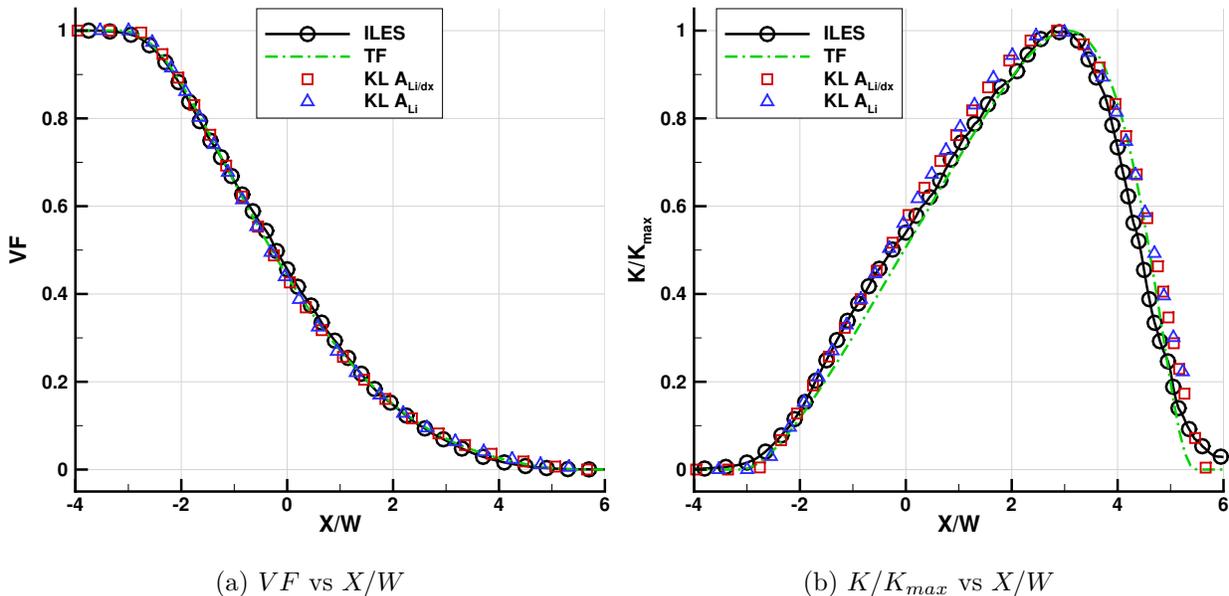
FIG. 18: Volume fraction (a) and normalized turbulent kinetic energy (b) profiles for RTI mixing of fluids with initial density ratio 20:1. Effect of local Atwood number term.

IV. CONCLUSIONS

Direct comparisons of the TF and K-L models were presented, for first time, in 1D engineering RT calculations of different initial density ratios. The comparison was additionally complemented by averaged ILES data [9]. The investigation covered a range of physical conditions; different initial interface pressures and specific heat ratios; examined the effect of grid resolution; the turbulent diffusion of enthalpy [48] vs. internal energy; and the calculation of the local Atwood number.

The turbulent diffusion of enthalpy formulated herein for the K-L turbulence model is shown to have a significant impact on the accuracy of the results, particularly for the maximum turbulent kinetic energy, K_{max}, and less for the integral mixing width, W. Furthermore, the profiles of the volume fraction (VF) and normalized turbulent kinetic energy (K/K_{max}) were also influenced by the enthalpy term.

The calculation of the Atwood number based on the values obtained during the reconstruction process, significantly improved the profile of K/K_{max}, while the limiting process based on the turbulent length scale L and the cell-width Δx improved the early-time self-similar growth rate of K_{max}, leading to results similar to the TF model.

The key findings from the comparison of the TF and K-L turbulence models are:

(a) $\bar{\rho}_1/\bar{\rho}_2 = 3$, $\alpha = 0.06$

(b) $\bar{\rho}_1/\bar{\rho}_2 = 20$, $\alpha = 0.08$
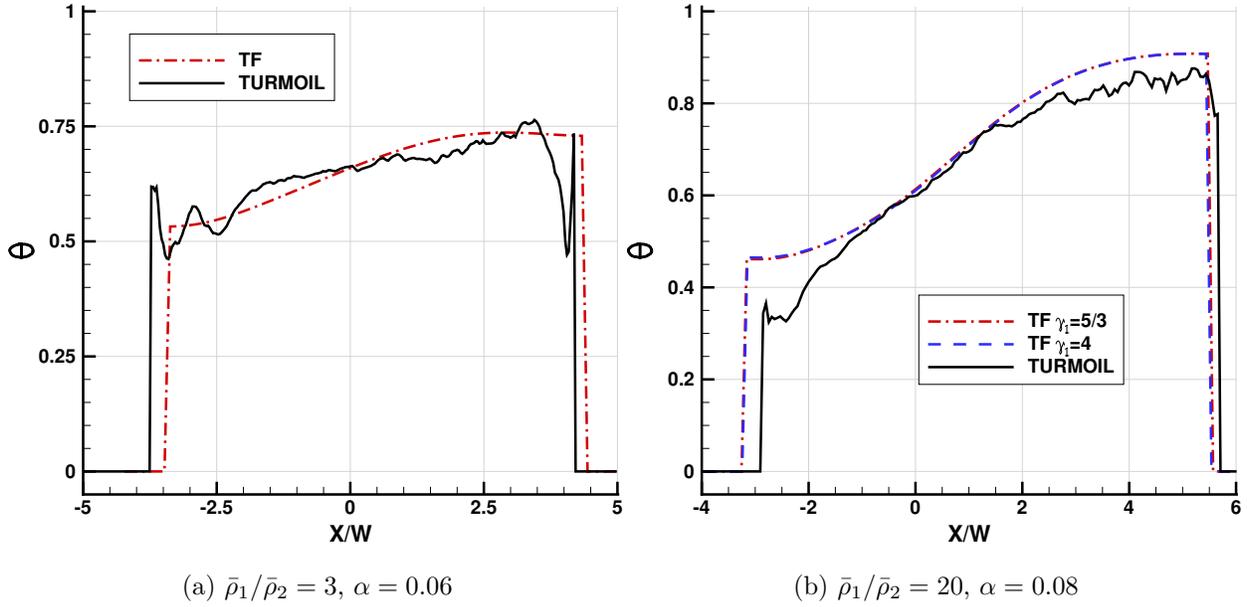
FIG. 19: Molecular Mixing Parameter $\theta(x)$ vs. x/W for density ratios 3 (a) and 20 (b) over 1; comparison of TF model with ILES (TURMOIL)

1. Both models achieve self-similarity.

2. Both models give similar results for the VF profiles;

3. the TF model overall predicts more accurately the K/K_{max} profile, especially at higher density ratios.

4. The mixing growth is similarly captured by both models, particularly at higher Atwood numbers.

5. Both models retain the same self similar growth rate for different heat capacity ratios (γ).

6. The TF model is less sensitive to changes of the initial interface pressure; small discrepancies in the K-L only appear at low density ratio (3:1) and initial interface pressure (250 dyn/cm^2).

7. The correct treatment of the enthalpy flux is needed in the K-L model in order to obtain temperature profiles, which are in good agreement with ILES and the TF model.

8. Changes in the procedure for the calculation of the local Atwood number in the *K-L* model led to self-similar growth rates that closely matched those obtained by ILES and the TF model, particularly at early time.

9. A key advantage of the TF model is that it is capable of representing the degree of molecular mixing in a direct way, by transferring mass between the two phases.

Finally, it is worth making a couple of comments on the numerical aspects. Simulations on finer grid resolutions result in less numerical dissipation [24, 56], which intertwines with the dissipation and diffusion explicitly provided by the turbulence model. This is a complex issue difficult to quantify in a priori manner. However, it is shown here that grid convergence is achieved provided that the dissipation and diffusion introduced by the model are of larger/similar magnitude to the corresponding numerical counterparts.

The present study provides an initial step towards a systematic comparison and a better understanding of single (two-equation) and multi-fluid models. The *K-L* mixing model uses a single velocity, which makes it numerically efficient and robust, but it precludes the description of de-mixing when the acceleration reverses sign. A comparison with ILES or DNS results for more complex test problems is considered essential for assessing the merits of the more advanced RANS models (TF or BHR [26]) over the relatively simple *K-L* model. The TF model has been successfully applied to more complex cases [19, 30] and further work is underway to obtain comparisons between the models for a range of 2D RM and RT problems pertinent to ICF applications, including investigation of the initial conditions and late-time mixing.

---

[1] P. Amendt, J. D. Colvin, R. E. Tipton, D. E. Hinkel, M. J. Edwards, O. L. Landen, J. D. Ramshaw, L. J. Suter, W. S. Varnum, and R. G. Watt, Physics of Plasmas **9**, 2221 (2002).

[2] J. Decaix and E. Goncalvès, International Journal for Numerical Methods in Fluids **68**, 1053 (2012), ISSN 1097-0363.

[3] J. R. Nanduri, D. R. Parsons, S. L. Yilmaz, I. B. Celik, and P. A. Strakey, Combustion Science and Technology **182**, 794 (2010).

[4] J. Ferziger, J. Koseff, and S. Monismith, Computers & Fluids **31**, 557 (2002), ISSN 0045-7930.

[5] A. S. Almgren, J. B. Bell, C. A. Rendleman, and M. Zingale, The Astrophysical Journal **637**, 922 (2006), URL http://stacks.iop.org/0004-637X/637/i=2/a=922.

[6] W. H. Cabot and A. W. Cook, Nature Physics **2**, 562 (2006).

[7] J. M. Pittard, S. A. E. G. Falle, T. W. Hartquist, and J. E. Dyson, Monthly Notices of the Royal Astronomical Society **394**, 1351 (2009).

[8] F. Grinstein, L. Margolin, and W. Rider, *Implicit large eddy simulation: computing turbulent fluid dynamics* (Cambridge Univ Pr, 2007).

[9] D. L. Youngs, Philosophical Transactions of the Royal Society A: Mathematical, Physical and Engineering Sciences **371** (2013).

[10] F. Grinstein, A. Gowardhan, and J. Ristorcelli, Philosophical Transactions of the Royal Society A: Mathematical, Physical and Engineering Sciences p. 371 (2013).

[11] D. Drikakis, M. Hahn, A. Mosedale, and B. Thornber, Philosophical Transactions of the Royal Society of London A: Mathematical, Physical and Engineering Sciences **367**, 2985 (2009), ISSN 1364-503X.

[12] B. Thornber, D. Drikakis, D. L. Youngs, and R. J. R. Williams, Journal of Fluid Mechanics **654**, 99 (2010), ISSN 1469-7645.

[13] U. Alon, J. Hecht, D. Ofer, and D. Shvarts, Physical review letters **74**, 534 (1995).

[14] B. Cheng, J. Glimm, and D. H. Sharp, Chaos: An Interdisciplinary Journal of Nonlinear Science **12**, 267 (2002).

[15] G. Dimonte and M. Schneider, Physics of Fluids **12**, 304 (2000).

[16] J. D. Ramshaw, Physical Review E **58**, 5834 (1998).

[17] J. C. V. Hansom, P. A. Rosen, T. J. Goldack, K. Oades, P. Fieldhouse, N. Cowperthwaite, D. L. Youngs, N. Mawhinney, and A. J. Baxter, Laser and Particle Beams **8**, 51 (1990), ISSN 1469-803X.

[18] D. Youngs, Physica D: Nonlinear Phenomena **37**, 270 (1989).

[19] D. Youngs, Laser and Particle Beams **12**, 725 (1994), ISSN 1469-803X.

[20] Y. Chen, J. Glimm, D. H. Sharp, and Q. Zhang, Physics of Fluids **8**, 816 (1996).

[21] A. Llor, *Statistical Hydrodynamic Models for Developing Mixing Instability Flows* (Springer, 2005).

[22] G. Dimonte and R. Tipton, Physics of Fluids **18**, 085101 (pages 22) (2006).

[23] S. Gauthier and M. Bonnet, Physics of Fluids A: Fluid Dynamics **2**, 1685 (1990).

[24] J. T. Morán-López and O. Schilling, High Energy Density Physics **9**, 112 (2013), ISSN 1574-1818.

[25] J. Morán-López and O. Schilling, Shock Waves **24**, 325 (2014), ISSN 0938-1287.

[26] D. Besnard, R. Rauenzahn, and F. Harlow, in *Computational Fluid Dynamics; Proceedings of the International Symposium*, edited by G. de Vahl Davis and C. Fletcher (1988), vol. 1, pp. 295–304.

[27] A. Banerjee, R. A. Gore, and M. J. Andrews, Physical Review E **82**, 046309 (2010).

[28] N. A. Denissen, B. Rollin, J. M. Reisner, and M. Andrews, in *43rd Fluid Dynamics Conference* (American Institute of Aeronautics and Astronautics, 2013), ISBN 978-1-62410-214-1.

[29] D. Youngs, Proceedings of the 5th International Workshop on the Physics of Compressible Turbulent Mixing pp. 83–88 (1995).

[30] D. L. Youngs, Philosophical Transactions of the Royal Society of London A: Mathematical, Physical and Engineering Sciences **367**, 2971 (2009), ISSN 1364-503X.

[31] K. Sinha, K. Mahesh, and G. V. Candler, Physics of Fluids **15**, 2290 (2003).

[32] D. Klem, in *Proceedings of the 9th International Workshop on the Physics of Compressible Turbulent Mixing*, edited by S. Dalziel (Cambridge University, Cambridge, UK, 2004), URL http://www.damtp.cam.ac.uk/iwpctm9/proceedings/IWPCTM9/Papers/Klem/Paper.pdf.

[33] G. Allaire, S. Clerc, and S. Kokh, Journal of Computational Physics **181**, 577 (2002), ISSN 0021-9991.

[34] A. Mosedale and D. Drikakis, Journal of Fluids Engineering, Transactions of the ASME **129**, 1497 (2007).

[35] P. Ramaprabhu and M. J. Andrews, Journal of Fluid Mechanics **502**, 233 (2004), ISSN 1469-7645.

[36] G. Dimonte, D. L. Youngs, A. Dimits, S. Weber, M. Marinak, S. Wunsch, C. Garasi, A. Robinson, M. J. Andrews, P. Ramaprabhu, et al., Physics of Fluids (1994-present) **16**, 1668 (2004).

[37] B. van Leer, Journal of Computational Physics **23**, 276 (1977), ISSN 0021-9991.

[38] V. Chiravalle, Laser and Particle Beams **24**, 381 (2006), ISSN 1469-803X.

[39] D. L. Youngs, Physics of Fluids A: Fluid Dynamics **3**, 1312 (1991).

[40] S. Godunov, Mat. Sb **47**, 134 (1959).

[41] K. Kim and C. Kim, Journal of Computational Physics **208**, 570 (2005).

[42] B. Thornber, A. Mosedale, D. Drikakis, D. Youngs, and R. R. Williams, Journal of Computational Physics **227**, 4873 (2008), ISSN 0021-9991.

[43] E. Toro, M. Spruce, and W. Speares, Shock waves **4**, 25 (1994), ISSN 0938-1287.

[44] D. Drikakis and W. Rider, *High - Resolution Methods for Incompressible and Low Speed Flows* (Springer, 2005).

[45] M. Hahn and D. Drikakis, International Journal for Numerical Methods in Fluids **47**, 971 (2005), ISSN 1097-0363.

[46] M. Hahn, D. Drikakis, D. L. Youngs, and R. J. R. Williams, Physics of Fluids **23** (2011).

[47] E. Shapiro and D. Drikakis, Journal of Computational Physics **210**, 584 (2005).

[48] A. W. Cook, Physics of Fluids **21**, 055109 (2009).

[49] F. A. Williams, *Combustion Theory* (Perseus Books, 1994), ISBN 9780201407778.

[50] D. Livescu, Philosophical Transactions of the Royal Society A: Mathematical, Physical and Engineering Sciences **371** (2013).

[51] P. Dimotakis, Journal of Fluid Mechanics **409**, 69 (2000), ISSN 1469-7645.

[52] N. Mueschke, O. Schilling, D. Youngs, and M. Andrews, Journal of Fluid Mechanics **632**, 17 (2009).

[53] D. Livescu and J. R. Ristorcelli, Journal of Fluid Mechanics **605**, 145 (2008), ISSN 1469-7645.

[54] D. Livescu, J. R. Ristorcelli, R. A. Gore, S. H. Dean, W. H. Cabot, and A. W. Cook, Journal of Turbulence **10**, 1 (2009).

[55] D. Livescu and J. Ristorcelli, in *Advances in Turbulence XII*, edited by B. Eckhardt (Springer Berlin Heidelberg, 2009), vol. 132 of *Springer Proceedings in Physics*, pp. 545–548, ISBN 978-3-642-03084-0.

[56] M. Latini, O. Schilling, and W. S. Don, Journal of Computational Physics **221**, 805 (2007), ISSN 0021-9991.